Journal of Alloys and Compounds 1057 (2026) 186907

Contents lists available at ScienceDirect

Journal of Alloys and Compounds

journal homepage: www.elsevier.com/locate/jalcom

Water-assisted grown ZnO transparent conductive oxide enables efficient thin-film solar cells

Stefano Pasini [a,*], Andrea Baraldi [a], Ildikò Cora [e], Gianluca Foti [a], Muhammad Kashif [a], Francesco Mezzadri [b,c], Ifeanyi John Onuorah [a], Antonella Parisini [a], Béla Pécz [e], Samaneh Shapouri [a,d], Giovanna Sozzi [d], Donato Spoltore [a], Alessio Bosio [a]

[a] Department of Mathematical, Physical and Computer Science, University of Parma, Parma 43124, Italy
[b] CNR-IMEM, Parco Area delle Scienze 37/A, Parma I-43124, Italy
[c] Department of Chemistry, Life Sciences and Environmental Sustainability, University of Parma, Parco Area delle Scienze 11/A, Parma I-43124, Italy
[d] Department of Engineering and Architecture, University of Parma, Parco Area delle Scienze, 181/A, Parma 43124, Italy
[e] Institute for Technical Physics and Materials Science, Centre for Energy Research, HUN-REN, Budapest H-1525, Hungary

ARTICLE INFO

Keywords:
TCO
ZnO
Sputtering
Solar cells
DFT

ABSTRACT

We report the development of a novel water-assisted growth ZnO (HZO) transparent conductive oxide (TCO) deposited by reactive d.c. magnetron sputtering in $Ar/O_2/H_2O$ atmosphere. Controlled water dosing acts as a surface surfactant, promoting c-axis oriented columnar grains with enhanced crystallinity and superior carrier transport properties. The HZO films exhibit high optical transparency across the visible spectrum ($E_g = 3.28$ eV) and low resistivity arising from degenerate conduction mechanisms. Electron mobility exceeds 30 $cm^2V^{-1}s^{-1}$ and the carrier concentration is on the order of 10^{19} cm^{-3}, consistent with a Burstein-Moss blue-shift partially compensated by band-gap renormalization.

Density Functional Theory (DFT) supports these findings, elucidating the electronic origin of the Fermi level shift and the interplay between band filling and defect. When integrated as a front contact in Sb_2Se_3-based solar cell, HZO matches or surpasses conventional ITO or aluminum doped ZnO contacts, improving short circuit current (J_{sc}) and reducing series resistance due to enhanced light scattering and charge transport. In short, rather than inserting an additional buffer layer, a single HZO layer can directly serve as the TCO, thereby eliminating the free-carrier absorption often seen in ITO as well as the In/Al contamination issues commonly associated with ITO- and AZO-based stacks.

The combination of environmentally friendly elements, scalable low-cost manufacturing, and exceptional optoelectronic properties make HZO a promising next-generation TCO solution for sustainable energy technologies.

1. Introduction

Transparent Conductive Oxides (TCOs) constitute a unique class of semiconductors that combine two properties rarely found simultaneously in a single material: high optical transparency in the visible spectral range and good electrical conductivity. These characteristics make them indispensable in a wide variety of optoelectronic and energy-related technologies, including flat-panel displays, light-emitting diodes, touch screens and thin film photovoltaics [1,2]. In the case of photovoltaic devices, the front electrode must fulfil a dual role. On the one hand, it should allow the incoming solar radiation to reach the active absorber layer without significant parasitic absorption, which requires an average transmittance above 80–90 % in the visible range. Such high transparency implies an electronic bandgap exceeding 3.0–3.1 eV, ensuring that photons in the visible spectrum do not promote interband transitions [3]. On the other hand, the front contact must also serve as an efficient current collector, which translates into an electrical conductivity on the order of 10^4 Scm^{-1} [4]. The simultaneous realization of these two conditions is not trivial, since generally a large bandgap oxide in its intrinsic state behaves as an electrical insulator at room temperature (RT). This apparent contradiction can be overcome by introducing sufficiently high levels of extrinsic doping. At moderate

* Corresponding author.
E-mail address: stefano.pasini@unipr.it (S. Pasini).

https://doi.org/10.1016/j.jallcom.2026.186907
Received 30 December 2025; Received in revised form 9 February 2026; Accepted 17 February 2026
Available online 18 February 2026
0925-8388/© 2026 The Author(s). Published by Elsevier B.V. This is an open access article under the CC BY license (http://creativecommons.org/licenses/by/4.0/).

doping concentrations, donor impurities generate discrete electronic levels just below the conduction band minimum. However, once dopant concentration exceeds the Mott critical density, these donor states begin to overlap and eventually merge with the conduction band. Under these degenerate conditions, the Fermi level is pushed inside the conduction band, and charge carriers occupy states even at thermal equilibrium. The material thus exhibits metallic-like conductivity while preserving a wide band gap. An additional optical consequence of degeneracy is the Burstein-Moss (B-M) effect. [5].

The most common TCOs used for the fabrication of thin-film solar cells are: In_2O_3:Sn indium tin oxide (ITO), SnO_2:F fluorine tin oxide (FTO), ZnO:Al aluminium zinc oxide (AZO) and Cd_2SnO_4 cadmium stannate (CTO). ITO is widely used in industrial applications such as plasma technologies, flat panel displays and solar cells [6]. Furthermore, the intensive use of this material has raised concerns about its future availability [7]. Another widely used TCO is zinc oxide (ZnO). The doping strategy for this semiconductor involves Al. Composite targets of AZO (Aluminum Zinc Oxide) consisting of (96−98) at% ZnO and (4−2) at% Al_2O_3 are commonly used for the sputtering of thin film of AZO. Since Zn is much more common on earth crust than In, the supply risk of this material is significantly lower than ITO. However, standard AZO is not free from critical drawbacks. The heavy extrinsic doping required to achieve low resistivity increases ionized-impurity scattering, which can limit the maximum attainable carrier mobility [8]. Furthermore, Aluminum redistribution/diffusion has been reported during elevated temperatures processing steps commonly used in thin-film solar cell fabrication, Al atoms may migrate within the device stack and, in some cases, reach the absorber layer, potentially introducing recombination-active defects and degrading the junction quality. This concern can motivate the insertion of protective High Resistivity Layers (HRL) or more complex buffer stacks, increasing device architecture complexity [9]. Consequently, developing a highly conductive, intrinsic-like ZnO TCO that relies on structural ordering rather than heavy extrinsic doping is of significant technological interest. The overarching goal of this work is to replace conventional doped TCOs (ITO, AZO, FTO) with a standalone, undoped ZnO-based electrode, thereby avoiding extrinsic metal doping and mitigating concerns about dopant incorporation/diffusion into adjacent functional layers. The objective is reach by introducing an H_2O-assisted growth ZnO (HZO), a ZnO thin film grown by reactive d.c. magnetron sputtering in an Ar/O_2 atmosphere with controlled H_2O partial pressure. HZO exhibits high optical transparency in the visible region of the solar spectrum, a wide band gap (~3.3 eV), low resistivity and high mobility, making it suitable for TCO applications. The figure of merit, defined as the ratio between the very low frequency conductivity and the optical conductivity, will be reported in the appropriate section, highlighting how this ratio assumes a very high value, characteristic of a TCO that is highly transparent in the visible light spectrum, and which simultaneously shows excellent electrical conductivity.

The process begins with a zinc target placed in a sputtering chamber where, in addition to the inert bombardment gas (argon), a controlled partial pressure of oxygen and water vapor are introduced. This approach is low-cost and easily scalable at an industrial level [10], facilitating rapid commercialization. Although hydroxyl-mediated ZnO growth has been previously reported using different deposition techniques such as ALD, sol–gel and humidity-assisted physical vapor deposition, where water mainly acts as an oxidant or surface modifier [11,12], the present work differs in several key aspects. In particular, we intentionally introduce H_2O as a controlled reactive species during DC magnetron sputtering, enabling a surfactant-like growth regime that is compatible with large-area and industrial processes [13]. Moreover, unlike previous studies that primarily focused on qualitative improvements in crystallinity or defect passivation, we establish a coupled static–dynamic kinetic model supported by DFT calculations to identify an optimal –OH surface coverage window. This framework allows us to directly correlate growth chemistry with microstructure, carrier mobility, and device-level performance.

Cross-sectional TEM reveals vertically oriented ZnO columnar grains with (001) preferred texture as confirmed by XRD. Electro-optical characterization was performed through Hall effect and absorption spectroscopy. The characterization has shown that the ZnO film deposited by reactive sputtering under optimized parameters, exhibits a non-uniform surface which leads to light diffusion (diffuse-fraction proxy), as confirmed by optical measurements. To the best of our knowledge, this specific morphology resulting from the reactive sputtering process has not been reported under comparable conditions.

Finally, we demonstrate device-level functionality by integrating HZO as front contact in a Sb_2Se_3 thin-film solar cell and benchmarking its performance against otherwise identical devices fabricated with standard ITO. We report the photovoltaic parameters and rationalize performance differences using the figure of merit (FoM). Both series of solar cells were fabricated and tested in-house under identical processing conditions [14].

In summary this work:

- Establishes a water-assisted reactive d.c. magnetron sputtering route for ZnO (HZO) within a stable, scalable process window.
- Reveals a ZnO texture morphology (diffuse-fraction proxy) emerging in sputtered films and evaluates its impact on TCO figure of merit.
- Demonstrates device-level performance in Sb_2Se_3 solar cells under like-for-like processing against ITO.

2. Experimental section

2.1. TCOs deposition

An ITO-based transparent conductive oxide was deposited by DCMS onto 1 in^2 soda-lime glass (SLG) substrates. Before deposition, the substrates were cleaned in acetone and isopropyl alcohol solution and subsequently sonicated for 10 min. The base pressure in the sputtering chamber was 1.5×10^{-6} mbar.

The TCO stack consisted of two layers. The first layer was a 900 nm ITO film deposited from a ceramic target composed of 90 % In_2O_3 and 10 % SnO_2. The deposition was carried out in an Ar + O_2 atmosphere, where O_2 accounted for 2.5 % of the total gas flow. After the introduction of oxygen, the partial pressure in the chamber was about 10^{-5} mbar, while after the addition of argon the working pressure reached 10^{-3} mbar. During deposition, the substrate was heated to approximately 500 °C, and a power density of 1.75 W/cm^2 was applied, resulting in a deposition rate of about 11 Å/s.

The second layer was a 120 nm intrinsic ZnO (i-ZnO) film made by d.c. reactive sputtering from a high-purity (99.999 % of purity) Zn metal target. The process used a gas mixture of argon and 15 % oxygen, with conditions like those for ITO. The substrate temperature was kept at 400 °C, the applied power density was 1. 56 W/cm^2, and the film was deposited at a rate of about 2. 2 Å/s. The i-ZnO layer served as a transparent, high-resistivity oxide, finishing the TCO stack. HZO-based TCO was deposited by sputtering onto soda-lime glass (SLG) substrates equivalent to those used for the ITO-based TCO. The substrates were cleaned following the same procedure described above. The structure consisted of a 450 nm thick In_2O_3 film, followed by a 1 μm thick HZO layer.

For the In_2O_3 layer, the same deposition conditions as for the ITO layer were employed, except for the applied power density, which was set to 0.66 W/cm^2. Under these conditions, the deposition rate was approximately 3.6 Å/s.

For the HZO layer, the deposition was carried out at a substrate temperature of 300 °C. The working atmosphere was obtained by introducing 20 sccm of Ar, 3.5 sccm of O_2 and 0.6 sccm of $H_2O(g)$ (starting from deionized water vapor 0.1 μs/cm) into the sputtering chamber, resulting in a total working pressure of 5×10^{-3} mbar. The O_2 flow corresponded to a partial pressure of about 8×10^{-5} mbar, while the

H_2O(g) flow contributed up to 9×10^{-5} mbar. During this process, a power density of 1.23 W/cm^2 was applied, yielding a deposition rate of approximately 4.5 Å/s.

Thicknesses of all layers were determined by measuring the deposition rate using a quartz micro-balance and the starting vacuum was 2×10^{-6} mbar for all depositions. We deposited HZO by RDMS, on sapphire (cleaned as described above) for electro-optical measurements, rather than on glass. As a reference we also deposited an intrinsic ZnO (i-ZnO) film on sapphire using the same DCMS conditions as those employed for the ITO-based TCO.

2.2. Solar cell fabrication

Sb_2Se_3 based solar cells were realized in superstrate configuration, where illumination occurs through the TCO substrate. To establish an optimized interface for charge separation and transport a bi-layer buffer consisting of CdS and $Zn_{0.2}Cd_{0.8}S$ was deposited by r.f. magnetron sputtering. The active absorber, Sb_2Se_3, was then deposited by Close Spaced Sublimation (CSS) of in Ar atmosphere. The heating stage (Crucible-Substrate) is carried out after introducing an argon pressure of 800 mbar to avoid any undesired sublimation. The substrate is heated to 360 °C, while the crucible is heated to 525 °C. To ensure a good thermalization, the heating process takes one hour. The growth of antimony selenide is performed under an argon back pressure of 0.1 mbar for a total deposition time of 10 min. These parameters ensure a film thickness of approximately 4 μm [14].

On the rear side, an oxygen-rich FeSO (Fe-S-O) film was used to improve hole extraction and simultaneously enhancing interfacial stability [10]. Finally, a gold layer was employed as metallic back-contact providing a reliable and low resistance electrical pathway. Both the Fe–S–O and Au layers were deposited by d.c. magnetron sputtering under carefully controlled conditions.

Detailed information regarding the deposition parameters and processing conditions can be found in our previous publications [10,14].

2.3. Device and film characterization

Optical, electrical, and structural characterizations were performed to assess the properties of the individual layers and the complete devices.

Optical absorption spectra of the TCOs (HZO and i-ZnO) were measured with a Shimadzu UV-3600i Plus spectrophotometer in the UV and visible light range with bare sapphire substrates as reference. The double-beam configuration compensates for the substrate contribution and instrumental baseline.

The HZO and i-ZnO films were analysed for electrical properties with a Keithley Hall system using the van der Paw geometry. 50 nm thick gold films were deposited by d.c. sputtering. The HZO and i-ZnO samples were prepared defining the device area with a stencil-type mechanical mask with a 6.5 mm diameter central hole and using an additional mask with four 1.5 mm diameter holes arranged along the edge of the main circle to geometrically define the contacts. This configuration was used to ensure that each small contact directly touched the HZO film, respecting as closely as possible the requirement imposed by the van der Paw method of having point-like contacts at the boundary of the device area. Hall effect measurements were performed in dark using a Keithley Hall Effect System at different temperatures in the range 10–300 K and by applying a 0.8 Tesla magnetic field perpendicular to the sample surface to record the Hall voltage. This allowed us to derive the carries density, their mobility and resistivity.

X-Ray diffraction data for i-ZnO and HZO was collected using a Rigaku Smartlab XE diffractometer with parallelized CuK_α incident beam. The measurements were carried out in grazing incidence geometry, with beam shaped into a 0.5 mm spot. A HyPix3000 detector was operated in 2D mode to acquire out-of-plane scattering information related to the texture of the sample. The 2D data were then integrated into a standard intensity vs 2θ plot.

Transmission electron microscopy (TEM) experimental data were collected in a spherical aberration corrected Titan Themis G2 200 (Thermo Fisher Scientific) (S)TEM equipped with an X-field emission gun (FEG) operating at 200 keV and 4k × 4k CETA16 CMOS camera (Thermo Fisher Scientific). Cross-sectional TEM lamellae were prepared by the focused ion-beam (FIB) technique using a ThermoFisher Scios 2 Dual Beam microscope (Eindhoven, The Netherlands) with EasyLiftTM nanomanipulator. Plan-view lamellae were prepared by conventional Ar-ion milling using Technoorg Linda ion miller. Energy dispersive X-ray spectrometry (EDS) elemental maps were acquired with a "Super-X" detector system built into the microscope column.

The current–voltage (J-V) characteristics of the Sb_2Se_3 solar cell were measured under simulated AM1.5 G illumination using a LOT-Oriel solar simulator (Irvine, CA, USA), equipped with a 600 W xenon arc lamp. The light intensity was calibrated with a pyranometer (LSI Lastem), whose broad spectral response (285–3000 nm) ensured determination of the integrated irradiance. To verify consistency with standard conditions, the calibration was compared to the nominal AM1.5 G spectrum specified for the simulator. All measurements were performed at 25°C in accordance with standard test conditions (STC). The short-circuit current density (J_{sc}), was determined using a calibrated shunt resistor coupled to a Keithley 4200-SCS parameter analyzer (Solon, OH, USA).

Series and shunt resistances of the solar cell were extracted from the illuminated J–V characteristics using a differential-resistance approach. The differential resistance $r_d(V) = dV/dJ$ was calculated from the measured J–V curves (with J in mA·cm^{-2}; after numerical smoothing to reduce noise amplification in the derivative). $R_s$and R_{sh} were then obtained by linear fitting of $r_d(V)$in the high forward-bias region (close to V_{oc}) and in the low-bias region (close to J_{sc}), respectively. The same fitting windows and procedure were applied to all devices, and resistances are reported as area-normalized values (Ω·cm^2).

EQE measurements were performed using a custom-built setup provided with a 50 W halogen lamp coupled with a monochromator (10 nm bandwidth), The monochromatic beam was directed normally onto the solar cell, and the photocurrent was measured with a Keithley 2400 source meter. The spectral intensity at each wavelength was monitored with a calibrated Si-photodiode (Newport 818-vis) to account for the wavelength-dependent lamp output. The integrated Jsc from EQE was compared with the Jsc obtained from J-V curves to ensure consistency.

3. Result and discussion

3.1. Dynamic in sputtering glow discharge

We combine controlled H_2O dosing and pulsed-d.c. sputtering to grow HZO with strong crystalline orientation and micron-scale grains, much larger than in conventional O_2-only reactive sputtering of ZnO. Water tunes the surface –OH coverage into a narrow, surfactant-like window that lowers interfacial energy and reduces nucleation density, while pulsed d.c. (high frequency f, (low-moderate duty-cycle D) chiefly stabilizes the discharge and decouples rate control from coverage control. In our implementation the pulse amplitude weakly depends on the discharge-sustaining bias, so pulsing acts as a stability knob, and –OH management drives the crystallinity and grain coarsening. To rationalize the behavior at both the metallic Zn target and the growing HZO surface, we built a coupled surface-kinetics and semi-empirical deposition rate (DR) framework. This allows to link substrate temperature and plasma parameters (power density, H_2O fraction) to –OH surface coverage and DR during HZO sputtering. We use –OH (hydroxyl) coverage, rather than "OH^-," which implies solvated anions, to indicate chemisorbed hydroxyl species on the surface.

Our approach is based on two main models for the deposition process. The static model predicts the steady state; here's the static law with an explicit $\chi_M$term [15,16]

$$DR_\infty(x,P_d) = K\,J_i(x,P_d)\,\chi_M(x,P_d)\,(\frac{P_d}{P_{d,\min}})^b \quad (1)$$

where:

DR_∞ is the deposition rate (Å·s^{-1}).

x: H_2O fraction; unless noted, flow fraction $x = F_{H2O}/F_{tot}$ (sccm/sccm).

P_d: power density at the target (W•cm^{-2}); $P_{d,min}$ is a reference value.

J_i: ion flux to the target/cathode (m^{-2} s^{-1}); estimated from discharge conditions.

$\chi_M \in [0,1]$: metallicity index, the fraction of metal-bearing flux (Φ_M) within the total reactive flux ($\Phi_M + \Phi_O x$) at the surface: $\chi_M = \Phi_M/(\Phi_M + \Phi_O x)$.

K and b: process constants obtained by calibration.

Therefore DR_∞ depends on:

(i) particle supply to the surface (J_i)
(ii) composition of that supply (χ_M)
(iii) discharge intensity (P_d).

Eq. (1) defines the maximum deposition rate DR∞ as a function of discharge and target surface conditions (metallicity). This steady-state description does not consider the transient observed at the beginning of the deposition process. For this purpose, we introduce a dynamic formulation.

The dynamic model describes the evolution of the deposition rate over time, DR(t), using a logistic function. The temperature dependence of OH sticking is captured by this sigmoidal expression.

$$DR(t) = DR_0 + \frac{DR_\infty - DR_0}{1 + \exp[-k(t-t_0)]} \quad (2)$$

where:

DR_0 is the initial rate (Å·s^{-1}); K (s^{-1}) is the effective kinetic constant; t_0 (s) is the inflection time. The sigmoidal law captures target conditioning and surface-site competitions: early-time changes in reactive adhesion and metal/oxidant equilibrium produce a rapid increase that saturates as the surface and discharge reach a conditioned steady state.

Having characterized the target-side power/conditioning that governs DR(t), we now turn to the substrate-side surface chemistry, –OH sticking $s(T)$ and coverage θ_{OH}. This model is governed by two key equations: the dependence of the sticking coefficient (s) on temperature (T) and the adsorption/desorption rate law of the –OH.

$$s(T) = s_{min} + \frac{s_{max} - s_{min}}{1 + \exp\left(\frac{T-T_{50}}{\Delta T}\right)} \quad 0 \le s_{min} \le s_{max} \le 1 \quad (3)$$

For low T, s(T) tends asymptotically to s_{max}.

For high T, s(T) tends asymptotically to s_{min}.

T_{50} is the mid-transition temperature, and ΔT governs its slope. We bound the adhesion probability between s_{min} and s_{max}, which represent the lower and upper asymptotic limits at high and low temperatures, respectively. s_{max} captures the maximum accommodation of –OH on a receptive surface, while s_{min} accounts for residual capture on a hot surface. Both are dimensionless and constrained as $0 \le s_{min} < s_{max} \le 1$. To physically ground the observed DR(t), we formulate a framework in which target-side conditioning and transport (J_i,χ_M) set the rate, while a Langmuir –OH sticking/desorption model [17] supplies the substrate-side constraint on site availability. In this picture, the –OH coverage $\theta_{OH}(T,x,t)$ evolves as:

$$\frac{d\theta_{OH}}{dt} = k_{ads}(T,x)\,(1-\theta_{OH}) - k_{des}(T)\,\theta_{OH} \quad (4)$$

With adsorption and desorption rates:

$$k_{ads}(T,x) = \frac{\eta_{geo}\ \Phi_{OH}(x)\ s(T)}{N_s},\ k_{des}(T) = \nu \exp\left(-\frac{E_{des}}{k_B\,T_K}\right) \quad (5)$$

Where $x = F_{H2O}/F_{tot}$ indicates the fraction of H_2O in the discharge. If χ increases, the hydroxylating flux $\Phi_{OH}(x)$ increases, consequently $k_{ads}(T,x)$ increases. Direct in situ quantification of –OH coverage is beyond the scope of this work; θ_{OH} is used here as a mechanistic descriptor consistent with the experimentally observed process window. The relationship between the hydroxylating flux in the gas phase and the adsorption of –OH on the substrate surface is expressed by η_{geo}, a dimensionless parameter that expresses the capture efficiency which depends on the geometric and transport conditions; in fact, this parameter takes into account the line of sight/solid angle and the diffusion as a function of the total pressure along the target/substrate distance. The density of surface sites available for hydroxylation Ns (m^2), defines the scale of the single layer used for θ_{OH}. As a starting hypothesis, θ_{OH} is considered constant and it identifies the chemically active subset of the geometric sites of the lattice. Surface crystallography gives us an order-of-magnitude estimate of Ns ≈ 10^{19} m^{-2} which is consistent with coverages of 2–10 –OH /nm^2 (for the oxides); this gives a value of $\theta_{OH} = 1$ for the single layer fixing the coverage scale for the –OH.

Eq. (2) admits a closed-form solution (for initial coverage θ_0) [18,19].

$$\theta_{OH}(T,x,t) = \theta_{eq}(T,x) + [\theta_0 - \theta_{eq}(T,x)]\exp(-t/\tau(T,x)) \quad (6)$$

where the steady state and characteristic timescale are:

$$\theta_{eq}(T,x) = \frac{k_{ads}}{k_{ads}+k_{des}} \in [0,1], \quad \tau(T,x) = \frac{1}{k_{ads}+k_{des}}. \quad (7)$$

Here $\theta_{eq}(T,x) = k_{ads}/(k_{ads}+k_{des})$ is the steady-state –OH coverage where adsorption balances desorption, and $\tau(T,x) = 1/(k_{ads}+k_{des})$ is the relaxation time constant; after one τ the deviation $|\theta - \theta_{eq}|$ is 1/e (≈ 37 %), and the convergence to the steady state is ≈ 95 % complete within ≈ 3τ.

The pulsed plasma parameters (flow and adhesion) and the target-side power density are therefore translated into the fraction of sites on the substrate/film surface occupied by –OH that controls nucleation, i.e., the actual growth rate and crystallinity of HZO. This model addresses the competition between adsorption and desorption of the –OH species by providing both the steady state coverage, used to identify the model-estimated operating range (0.2–0.5 ML). Direct in situ quantification of –OH coverage is beyond the scope of this work; θ_{OH} is used here as a mechanistic descriptor consistent with the experimentally inferred process window, and the time-transient dependence on steady state growth. This description provides the missing link between growth rate and surface kinetics, avoiding over-hydroxylation and stabilizing the species composition on the HZO film surface under pulsed d.c. conditions. Langmuir kinetics, Eqs. (1–7), directly describes the family of $\theta_{OH}(T)$ curves. The adsorption rate $k_{ads}(T,x) = \eta_{geo}\,\Phi_{OH}(x)\,s(T)/N_s$, at fixed pressure and geometry, decreases with T because s(T) is limited and decreases with temperature. The desorption rate, however, $k_{des}(T) = \nu \exp(-E_{des})/(k_B T_K)$ increases with T. The ratio state $\theta_{eq}(T,x) = k_{ads}/(k_{ads}+k_{des})$ establishes the steady state, which decreases monotonically with temperature. At constant temperature, by changing x, the fraction of H_2O, the curves shift upward ($\Phi_{OH}(x)$ ⇒ higher k_{ads} ⇒ higher θ_{eq}). The power density variations, even with increasing reactive flux, have the same qualitative trend. The band between the red dashed lines (0.2–0.5 ML) shows the model-predicted coverage region in which nucleation is abundant without over hydroxylation. The intersection of the curves with the red dashed lines indicates an optimal temperature range between 300 and 350°C. Therefore, this is the ideal temperature window that allows an effective nucleation site density for enhanced crystal growth.

In Fig. 1(b) the static + dynamic model is highlighted: DR_∞ is

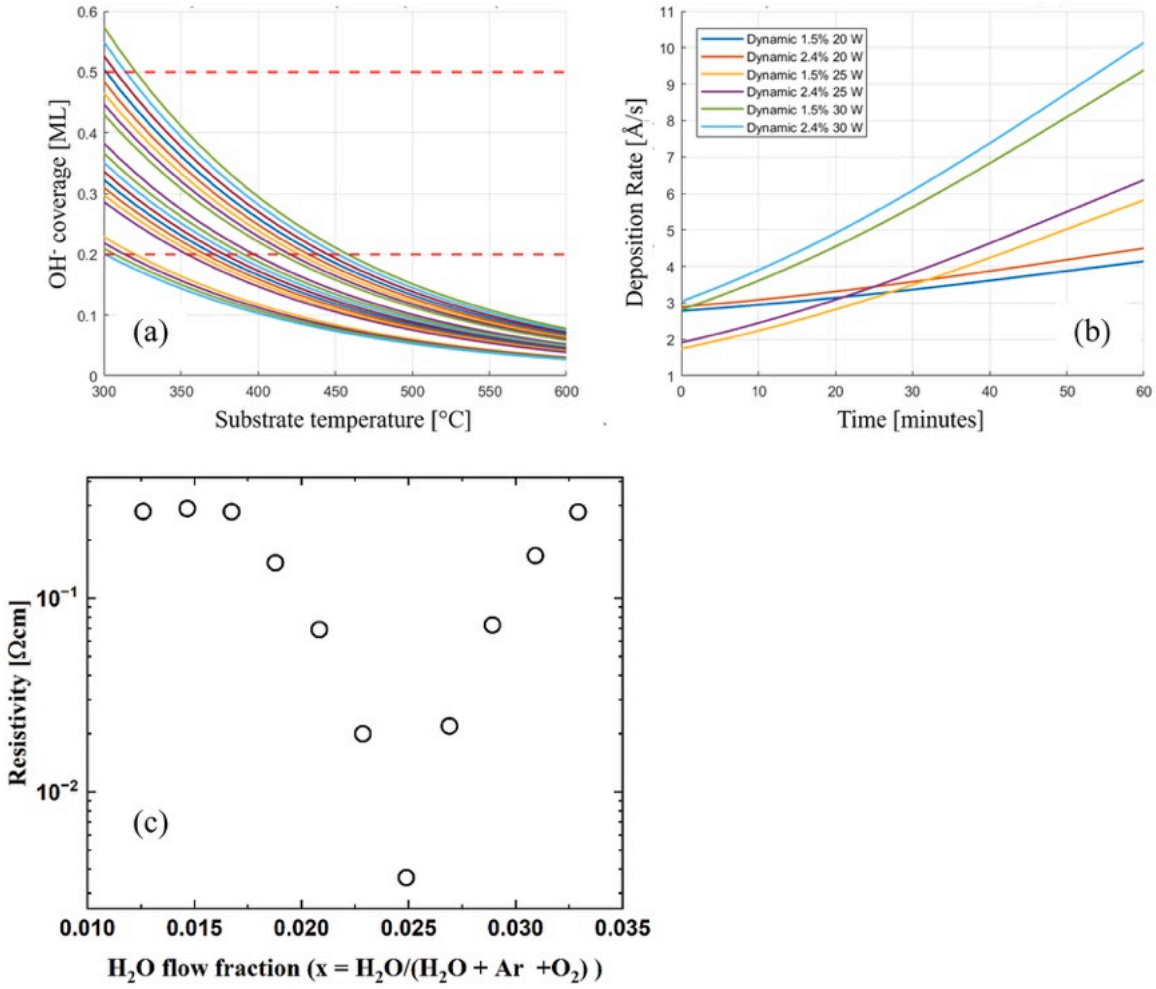


Fig. 1. (a) steady-state prediction from Eqs. (1 – 7) of the –OH coverage as a function of the absolute temperature; (b) transient behavior of the deposition rate (DR) as a function of time at fixed sputtering power and H_2O fraction (x) (equilibrium between target and film/substrate conditions); (c) Resistivity of HZO films as a function of H_2O flow fraction $x = F_{H2O}/F_{tot}$, measured for samples deposited at fixed substrate temperature T = 300 °C and fixed sputtering power density P = 1.23W/cm^2. The curve highlights a well-defined optimum x range, supporting a narrow H_2O dosing window.

obtained from the static part, in fact, within the operating window, the increase in power density P_d with a relative increase in the value of χ_M lead to an increase in DR_∞. Going from 20 to 30 W, reported with the corresponding P_d, the deposition rate increases depending on a modest increase in J_i and with an attenuation of the target oxidation which causes an increase in χ_M. The dynamic model shows a time trend towards steady state conditions: with $P_d = 30$ W and $x = 2.4$ % at 60 min deposition, $DR_\infty = 10$ Å/s, more than double the value obtained with $P_d = 20$ W. Furthermore, the static scale indicates that further increasing the power can trigger an instability drift in χ_M, while remaining within acceptable values. Considering a balance of these effects, the optimal ranges for HZO growth is 300–350°C for temperature, 20–25 W for power and $x = 1.5$ % – 3.0 % for the percentage of H_2O. These conditions preserve $\theta_{OH} \in [0.2, 0.5]$ ML stabilize χ_M and allow the production of HZO films of high crystalline quality and avoid over hydroxylation or metal drifts.

The presence of a moderate amount of –OH on the surface of the growing film acts as a surfactant by reducing the free energy at the film/substrate interface and thus increasing surface mobility. The increased surface diffusion length reduces the nucleation density by promoting lateral coalescence of crystalline grains, which results in the production of much larger grains for the same film thickness compared to a ZnO film deposited under the same conditions, but in the absence of H_2O. HZO films grown under optimal conditions have an average grain size of approximately 2 μm, while ZnO films grown without intentional H_2O have grains of approximately 20 nm.

An approximately hundredfold increase in grain size yields an ~10^4 reduction in island density, consistent with $N \propto 1/L^2$, where L is the mean lateral grain size and N the areal island/grain density.

This behavior suggests that between 300 and 350 °C, the surface diffusion barrier decreases, allowing for faster surface diffusion. High-quality films were obtained only when the surface coverage of –OH was maintained within a narrow window. Outside this range, the microstructure deteriorates:

- with too few –OH groups, numerous reactive sites remain, activating excessive nucleation and nanoscale grains.
- with too much –OH, steps and island edges become passivated, weakening adhesion and suppressing crystallization and texture development.

Within the optimal window, –OH does not directly affect the DR; instead, it modulates grain growth, explaining the higher crystallinity and coarser grains observed in HZO compared to water-free ZnO.

Additionally, we can explain how pulsed d.c. influences target stability, where high frequencies control transients and arcs, and average power aligns with peak power, affecting the deposition rate primarily through set d.c. flux and metallicity index. With a small pulse width (ΔV

= 15–20 V and Vdc= 3 00 V; ΔV<<Vdc), the pulsed d.c. regime acts primarily as a stability control mechanism on the target side. Higher frequency suppresses restrike transients and arc formation, and the duty cycle functions to translate peak power into a controlled average power; consequently, DR(t) is predominantly governed by the set d.c. flux J_i and the metallicity index χ_M, with only modest changes in average rate induced by pulsing. On the substrate side, the sheath potential is set by Vdc, so a narrow rectangular pulse introduces only minor perturbations. The time-averaged hydroxylation dose, and hence the –OH coverage θ_{OH}, is controlled predominantly by the fraction x of H_2O and the substrate temperature T, with a weak direct dependence on the pulsing frequency. The effect of electrical loading scales approximately with D·(ΔV/Vdc) and is generally negligible under these conditions. In practice, operating within the model-estimated $\theta_{OH} \in [0.2, 0.5]$ ML regime by adjusting x and T results in a mobility and consistency like those of surfactants (coarser and better HZO oriented crystalline grains), while the deposition rate remains determined by χ_M and J_i. In short, with ΔV≪Vdc, the pulsed mode stabilizes the discharge, while managing –OH (via x and T) determines crystallinity, clearly separating rate control from microstructure control. To verify that the H_2O-assisted growth is governed by a finite process window, we varied the H_2O flow fraction $x = F_{H2O}/F_{tot}$(here $x \approx 1.26\%–3.29\%$, with F_{Ar} = 20sccm and F_{O2} = 3.5sccm) at fixed substrate temperature (T = 300 °C) and sputtering power density (1.23 W/cm^2). Resistivity shows a clear dependence on x, with a minimum at intermediate dosing (Fig. 1(c)). These trends support an optimal H_2O dosing window consistent with the proposed kinetics-driven growth modification.

3.2. TCOs characterization

3.2.1. Optical measurements

The absorption spectrum of the novel TCO material is presented in Fig. 2(a) together with the one related to a film of intrinsic ZnO as reference. The low optical absorption in the visible range (1.6–3.1 eV) confirms the excellent transparency, a key requirement for application in solar photovoltaics. Tauc plot (following the baseline subtraction process indicated in [20,21]) analysis indicates that the band gap of HZO (3.28 eV) is approximately 20 meV higher than i-ZnO (3.26 eV).

Although this difference is close to the typical uncertainty of such an optical method, the result is consistent with the hypothesis of a B-M effect. As noted below, Hall effect measurements were performed independently to determine the carrier concentration, thus providing a more solid basis for evaluating the contribution of the B-M shift.

An integrating-sphere haze setup was not available; therefore, we do not report an absolute haze factor. Instead, we estimate a diffuse-fraction proxy from optical spectra, which captures relative forward-scattering trends. To estimate the wavelength-dependent diffuse-fraction proxy S(λ) in both samples we employed the model proposed in [22,23]:

$$S(\lambda) = \frac{T_{sp-id}(\lambda) - T_{tot}(\lambda)}{T_{tot}(\lambda)} \tag{8}$$

where $T_{tot}(\lambda)$ is the measured total transmittance and $T_{sp-id}(\lambda)$ is the ideal specular transmittance.

The latter is estimated by considering a plane-parallel film on a substrate, including the Fresnel reflections at the interfaces:

$$T_{sp-id}(\lambda) = (1 - R_1)(1 - R_2)e^{-\alpha d} \tag{9}$$

where (α) is the measured absorption coefficient, d is the film thickness and R_1 and R_2 are defined as:

$$R_1 = \left(\frac{n_{film} - n_{air}}{n_{film} + n_{air}}\right)^2; R_2 = \left(\frac{n_{sub} - n_{film}}{n_{sub} + n_{film}}\right)^2 \tag{10}$$

with $n_{film} = 2.0$ (refractive index of both i-ZnO and HZO) and $n_{sub} = 1.76$ (refractive index of the sapphire substrate) [24,25].

The average fraction of diffused light over the measured spectral range was then obtained as:

$$\overline{S} = \frac{1}{N}\sum_{i=1}^{N} S(\lambda_i) \tag{11}$$

where N is the total number of the spectral points.

The relative difference in optical diffusion between the HZO and i-ZnO was quantified as:

$$\Delta S_{\%} = 100 \cdot \frac{|\overline{S}_{HZO} - \overline{S}_{i-ZnO}|}{\overline{S}_{i-ZnO}} \sim 10\% \tag{12}$$

We stress that $S(\lambda)$ is a proxy derived from spectra (not an absolute haze measurement), and it is used here to compare scattering trends between samples.

This value indicates an enhancement of light scattering in the HZO likely induced by the H_2O presence during the sputtering process. Such a light-trapping phenomena, effectively increase the optical path length of incident photons within the absorber layer of the solar cell. Consequently, the probability of photon absorption increases, especially in the spectral range near the absorber's band edge, where the absorption coefficient is high. This effect is expected to contribute to an increase in short-circuit current density (J_{sc}) and thus could potentially improve the overall photovoltaic conversion efficiency.

3.2.2. Electrical measurements

In order to study the charge transport mechanism, Hall effect and resistivity measurements were performed, that reveal degenerate

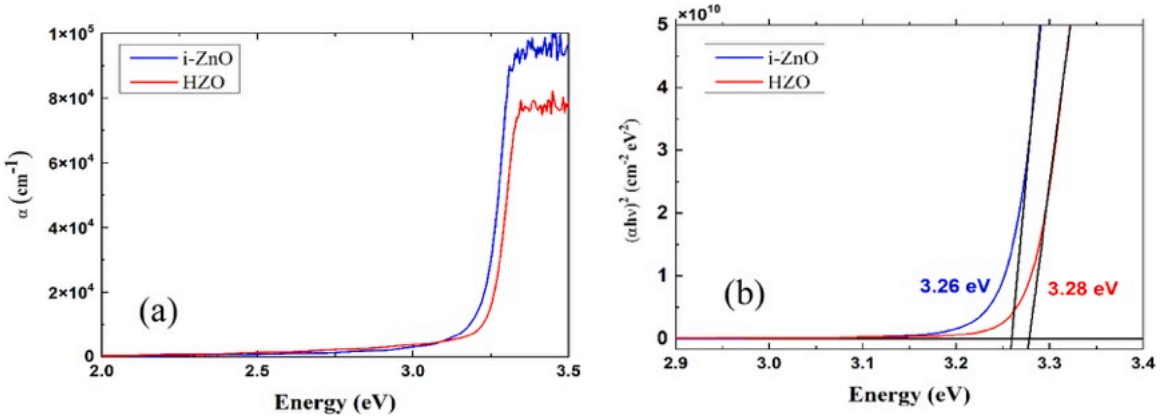


Fig. 2. (a) absorption coefficient of HZO (red) and i-ZnO (blue) as a function of the photon energy (eV); (b) Tauc plots for direct allowed transitions for HZO (red) and i-ZnO (blue) with the extrapolated E_g values.

transport in HZO and thermally activated/hopping conduction in i-ZnO. These differences can explain the optical band gap shift via the B-M and band gap renormalization effects. From Fig. (3a) it can be observed that resistivity remains nearly constant as a function of temperature in HZO (the experimental error on the resistivity is on the order of 5 %), consistently with a metallic-type conductivity. This conclusion is also supported by the nearly temperature-independent Hall effect data.

In contrast, the i-ZnO sample, Fig. 3b shows a thermally activated conduction in all the temperature range. At high temperature a linear dependence of ln(ρ) versus 1/T is observed with activation energy of (26.31 ± 1.48) meV. This behavior may indicate conduction via either extended states or nearest-neighbor hopping [26]. For conduction via extended states, the donor is modelled as a shallow hydrogenic defect. The corresponding donor level exhibits an activation energy of approximately 45.2 meV, as obtained from the well-established relation:

$$E_n = E_n(H)\left(\frac{m^*}{m_0}\right)\cdot\frac{1}{\epsilon_r^2} \tag{13}$$

where m* is the effective electron mass ($m^* = 0.24\ m_0$), ε_r (equal to 8.5) is the relative dielectric constant, and $E_n(H)$ denotes the Rydberg energy of the hydrogen atom for $n = 1$ [27,28]. The significant discrepancy between experimental activation energy and the value predicted by the hydrogenic model suggests that the high-temperature conduction mechanism in i-ZnO is not governed by extended states transport but is rather dominated by nearest-neighbor hopping.

However, such a difference could also indicate the formation of localized states at the bottom of the conduction band (CB) and the widening of the fundamental donor state into an impurity band (IB), so that the minimum distance from IB and CB bottom is significantly lower than the depth of the ideal fundamental state of the hydrogenic donor. However, mobility was found very low, as typical of hopping transport, and measurable only at RT.

At low temperatures, however, a different transport mechanism prevails. The data in the temperature range between 100 K and 12.5 K, (Fig. 3b), were fitted using the analytical equation:

$$y = mx^{\alpha} + q \tag{14}$$

where $y = \ln(\rho)$ and $x = 1/T$. The exponent α shows a value of (0.208 ± 0.063), which is in good agreement with the value of ¼ consistent with the Mott law:

$$\rho(T) = \rho_0 \exp\left[-\left(\frac{T_m}{T}\right)^{\frac{1}{4}}\right] \tag{15}$$

Here T_m is the characteristic temperature, expressed as

$$T_m = \frac{18}{K_B N(E_F)\xi^3} \tag{16}$$

where ξ is the localization length of the wavefunction.

This consistency indicates that within this temperature range, the conduction mechanism, is governed by Variable-Range Hopping (VRH) transport mechanism [29–32].

The slope (m) of the fit allows the determination of the characteristic temperature ($T_m \approx 39.36$ K). By combining T_m with the localization length of the wavefunction ξ, it is possible to extract key physical quantities [33]. These include:

- the electronic density of localized states available for hopping near the Fermi level $N(E_F)$:

$$N(E_F) \approx 2.46 \cdot 10^{22}\ eV^{-1}cm^{-3} \tag{17}$$

- the spatial separation between sites that participate in the hopping process $\overline{R}$:

$$\overline{R} \approx 5.64 \cdot T^{-1/4} nm \tag{18}$$

- the energy required for charge carriers to overcome the energy mismatch between neighboring localized states $\overline{w}$:

$$\overline{w} \approx 0.054 \cdot T^{3/4} meV \tag{19}$$

In disordered oxide semiconductors, and in polycrystalline or nanocrystalline ZnO films, the localization length associated with tail states can extend over several tens of angstroms due to structural disorder, granularity, and the presence of defects [34,35]. Experimental studies on ZnO nanocrystal films have further shown that the localization length can be determined via VRH fitting, assuming values on the order of a few nanometers [36,37]. Therefore, for the VRH conduction analysis in the present work, we adopt a realistic value of $\xi \approx 6$ nm, consistent with the range commonly reported in the literature for materials with strongly granular microstructures [35,36].

The chosen value of the localization length ξ is consistent with physical expectations. An estimation of the density of centres partici-

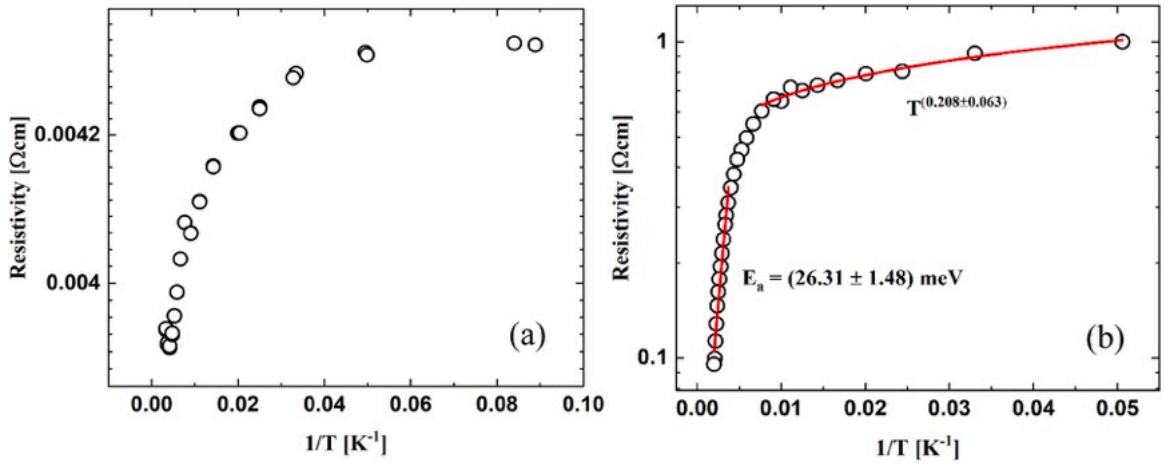


Fig. 3. Resistivity as a function of 1/T for (a) HZO and (b) i-ZnO. Note the different vertical scale. In (a) the variability of the resistivity remains within the experimental error. The red lines in (b) represent the data fitting.

pating in the hopping mechanism (*N*), expressed as [30]:

$$N = \left(\frac{4\pi\bar{R}^3}{3}\right)^{-1} \sim 4{\cdot}10^{19}\ cm^{-3} \tag{20}$$

is found to be of the same order of magnitude as the free carrier density determined from Hall effect measurements, supporting the plausibility of the assumed ξ.

Table 1 reports the results at Room Temperature (RT) extracted from Hall measurements for both HZO and i-ZnO.

The Hall effect measurements provide the carrier density, which can be used to estimate the B-M shift in the optical gap, justifying the difference in energy gap between the two samples shown in Fig. 2(b). In the case of a degenerate semiconductor (HZO sample), the difference between the optical bandgap due to band filling and the intrinsic bandgap is expressed as follows:

$$\Delta E_{BM} = \frac{\hbar^2(3\pi^2 n)^{2/3}}{2m_e^*} \tag{21}$$

where $\hbar$ is the reduced Planck constant, n is the free electron density, and m^*_e is the electron effective mass (0.24 m_0 for ZnO). From the experimental data in the table, the energy difference referred to the B-M effect is estimated to be about 171 meV, and this value turns out to be much larger than the measured increase in the optical gap. It is important to note that the gap extracted from Tauc analysis should be regarded as an apparent optical onset, which in degenerate and/or disordered ZnO can be affected by band-tail states (Urbach tails), disorder broadening and band nonparabolicity. Therefore, the measured $\Delta E_g$is not expected to match ΔE_{BM}alone, but rather the net shift $\Delta E_{net} = \Delta E_{BM} - \Delta E_{BGR}$ (plus tailing/non-parabolic corrections).

Furthermore, the optical band gap of a degenerate semiconductor can be expressed as [38]: $E_{g,optical} = E_g + \Delta E_{BM} - \Delta E_{BGR}$

In the case under study, the optical gap increase is ≈ 20 meV, compared with a calculated B-M shift of ≈ 171 meV. This discrepancy (≈151 meV) is attributed to the Band Gap Renormalization BGR effect. The BGR energy consists of two contributions: one related to the Coulombic interaction, expressed as [38,39]:

$$\Delta E_C = -\frac{e^2}{4\pi\epsilon_0\epsilon_{eff}}\left(\frac{3n}{\pi}\right)^{\frac{1}{3}} \sim 82 \quad meV \tag{22}$$

and an excitonic contribution following the Wannier-Mott model [40,41]

$$\Delta E_{WM} = \frac{\mu e^4}{2\left(4\pi\epsilon_0\epsilon_{eff}\right)^2\hbar^2} \sim 68 \quad meV \tag{23}$$

An effective dielectric constant of 5.82 was used, obtained as a weighted average between the static ($\varepsilon_0 = 9$) and optical ($\varepsilon_\infty = 3.7$) values, reflecting the polar nature of ZnO (approximately 60 %) [42] and μ is the reduced mass calculated from $m^*_e = 0.24\ m_0$ and $m^*_h = 0.59\ m_0$ [43–45]. By summing these two effects, a value of approximately 150 meV is obtained, which is in good agreement with the experimental observation. Thus, the observed $\Delta E_g$is consistent with a Fermi-level shift scenario (Burstein–Moss) largely compensated by BGR, with the apparent optical onset additionally influenced by tailing/nonparabolicity. Moreover, the lattice disorder in i-ZnO samples localizes energy states near the conduction band edge (weak Anderson localization), reducing the effective contribution of carriers to band filling. The product between the Fermi wavenumber k_F and the mean free path *l* is a dimensionless figure of merit widely used to identify the metal-to-insulator transition in metal oxides [46]:

$$k_F \bullet l = \frac{(3\pi^2)^{\frac{2}{3}}\hbar}{\rho e^2 n^{\frac{1}{3}}} \tag{24}$$

Physically, the dimensionless product $k_F \bullet l$ compares the mean free path $\underline{l}$ to the Fermi wavelength λ_F. For $k_F \bullet l >> 1$, electrons propagate as extended Block states and Drude model can be applied. When $k_F \bullet l \approx 1$, scattering is so frequent that electrons lose phase coherence within one wavelength, leading to the onset of Anderson localization and insulating behavior. According to this rule, known as the Ioffe-Regel criterion [47], conduction trough Block states become invalid when $k_F \bullet l \leq 1$. From Table 1 $k_F \bullet l = 2.74$ for HZO and 0.04 for i-ZnO, confirming that HZO behaves as a degenerate semiconductor, while i-ZnO lies deep in localized regime, consistent with its smaller optical band gap.

Table 1
Main results of Hall effect measurement at RT.

RT values	HZO	i-ZnO
ρ [Ω·cm]	$3.94 \cdot 10^{-3}$	$2.83 \cdot 10^{-1}$
μ [$cm^2\ V^{-1}\ s^{-1}$]	32.37	0.59
n [cm^{-3}]	$4.89{\cdot}10^{19}$	$3.76{\cdot}\ 10^{19}$
$k_F l$	2.73	0.04

3.2.3. *Structural characteristics*

Fig. 4 shows the XRD patterns of the i-ZnO and HZO samples. In both cases, the same crystal growth planes are observed (vertical blue dashed lines), while the additional unassigned peaks are attributed to the In_2O_3 buffer layer deposited on glass, which acts as a barrier against sodium diffusion from the substrate.

Moreover, the two XRD patterns exhibit a significant variation in the intensity of the reflections of the crystal planes. To quantify this variation and identify the preferential growth plane, the texture coefficient (TC) was calculated in both cases, defined as [48,49]:

$$TC_{hkl} = \frac{I_{hkl}/I^0_{hkl}}{\sum_{i=1}^{n} I_{h_i k_i l_i}/I^0_{h_i k_i l_i}} \cdot 100 \tag{25}$$

Here I_{hkl} represents the experimental height of the peak intensity of the n-th reflection labeled in Fig. 4, I^0_{hkl} is the intensity of the same reflection in the completely random powder, as reported in the reference, calculated using the crystallographic data for In_2O_3 (bixbyite phase, COD ID 1538147) and ZnO (wurtzite phase, COD ID 9008877).

The HZO thin film exhibits a pronounced preferential orientation perpendicular to the (001) growth plane, indicating that the grains are predominantly aligned along the c-axis. Such a growth mode may

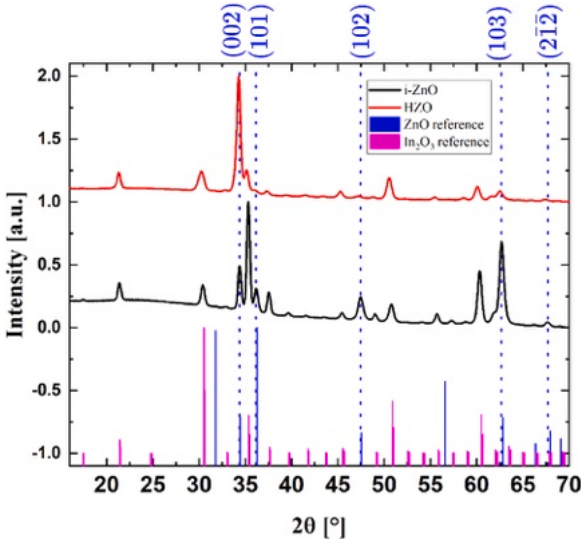


Fig. 4. XRD patterns of i-ZnO (black) and of HZO (red) thin films deposited on In_2O_3 buffer layer. In both cases In_2O_3-coated soda lime glass was used as substrates.

suggest the presence of nucleation centers characteristic of a ZnO nanowire-like structure. Conversely, the TC profile of the i-ZnO sample, shown in Fig. 5(b), reveals a more random grain orientation, lacking any significant preferential alignment.

The cross-sectional TEM analysis of the i-ZnO film deposited on sapphire reveals two distinct structural regions (Fig. 6a). The lower region, extending approximately 50–200 nm from the substrate, consists of small crystallites with pronounced texture. Most grains in this region exhibit a substrate-driven crystallographic correlation (For the sake of simplicity, we will henceforth adopt the term epitaxial), as substantiated by the corresponding SAED patterns (inset of Fig. 6a)

The upper part of the i-ZnO film, however, indicates a completely different morphology, consisting of large (50–300 nm wide x max. 1 μm long), well developed, V-shaped or columnar crystals, showing the loss of in-plane epitaxial relations towards the surface as shown by the SAED patterns (Fig. 6a). Nonetheless, the 002 peak in normal direction to the interface is retained, indicating a fibre-like texture. In order to see in-plane orientation relationships, we prepared a plan-view TEM lamella from the upper part of the sample. The SAED pattern (Fig. 7a), shows that the top of the layer is less textured, as close to the reflections of expected in the [001] zone axis, other spots appear, like 101, 202, 203, indicating that some crystals grow with the (002) plane not perfect parallel to the surface of the substrate. Bright field (BF) image of the layer (Fig. 7d) shows typical grain size of 50–300 nm (cross section of the elongated ZnO crystals) with mostly typical 120° grain boundary.

In contrast to i-ZnO, the HZO sample exhibit columnar grains oriented along the c-axis, maintained throughout the full film thickness of 850–1000 nm. (Fig. 6b).

The columnar ZnO grains are elongated along the c-axis and exhibit mainly epitaxial growth in cross sectional sample. In order to reveal the texture SAED patterns (7b-c) were acquired also from plan view sample, exhibiting the cross section of the columns. The ZnO columns are strongly textured, all the grains are in [001] projection with a slight rotation of each crystal around its c-axis. Such misorientation suggest the presence of minor local strain or relaxation mechanism during growth, which may lead to small-angle grain boundaries at the column interfaces. For further demonstration HRTEM image with the corresponding FFT from plan view sample presents 3 grains (cross section of columns) with equilibrial ~120° triple grain boundary and the ~8.3° and ~16.6° low angle boundaries between individual grains. The typical diameter of the columns is 50–300 nm (Fig. 7e).

The epitaxial growth is confirmed from cross sectional TEM sample, as well by high-resolution TEM images (Fig. 8), concluding that small rotations around the c-axis do not appreciably modify the overall texture. No detectable amorphous phase was identified by HRTEM as

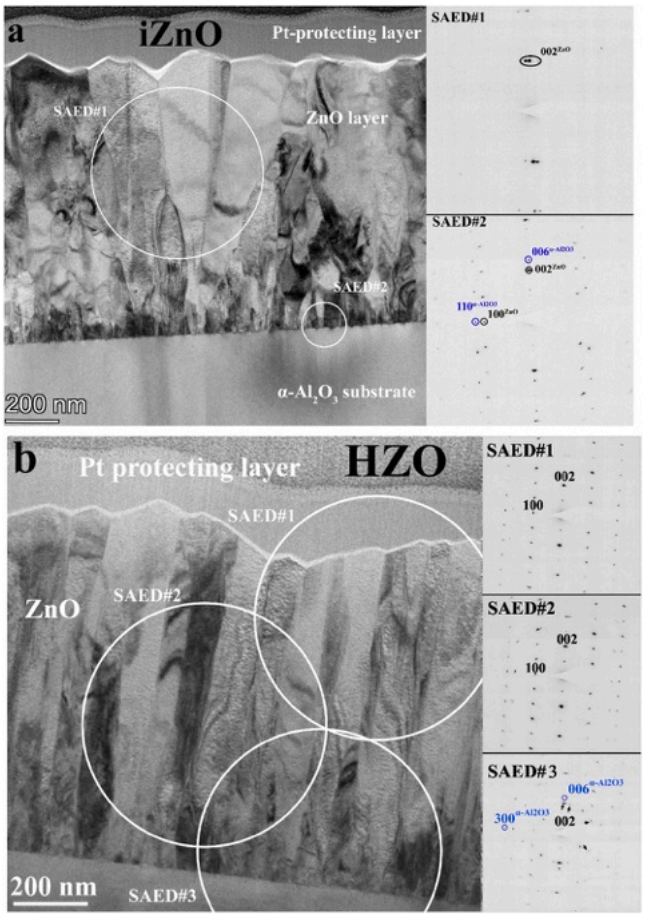


Fig. 6. Bright-field (BF) TEM image of the layer with corresponding SAED patterns acquired from the marked areas (white circles) from a) iZnO and b) HZO samples. a) The lower part of the iZnO layer shows mainly epitaxial grains, while the upper part of the layer is less structured and the crystals are not in epitaxial relationship with the substrate. b) HZO layer consists of columnar ZnO grains elongated along the c axis, perpendicular to the substrate surface. These columns exhibit a small relative in-plane rotation, consistent with a modest mosaic spread of the layer. No detectable amorphous phase was observed in the inverted SAED patterns.

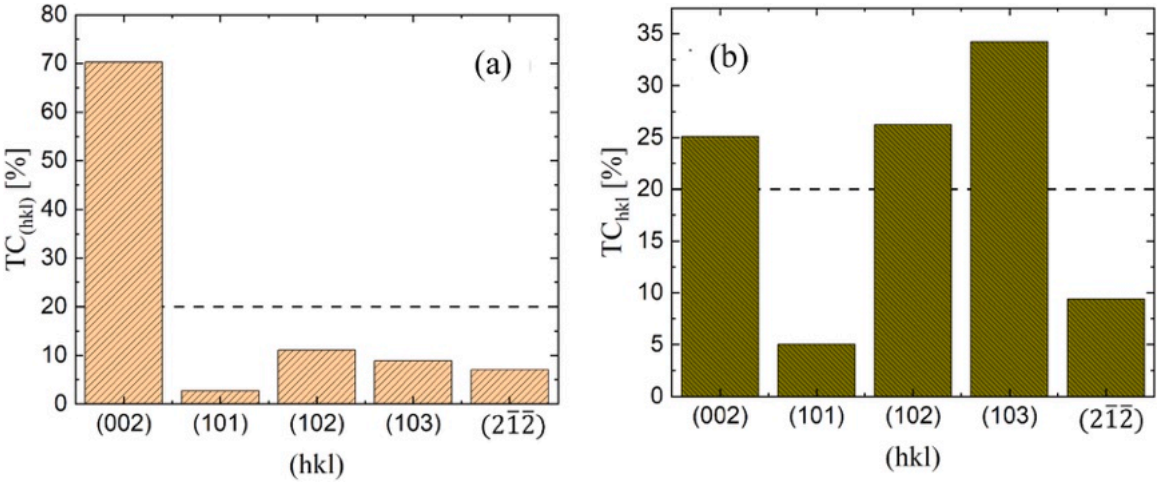


Fig. 5. Texture coefficient TC (hkl) for the crystalline planes shown. (a) A strong (001) texture is evident, while the remaining planes show reduced intensity (HZO). (b) No dominant texture is observed (iZnO). A crystal plane was considered non-negligible when its TC exceeded 20 %, as indicated by the dashed horizontal line.

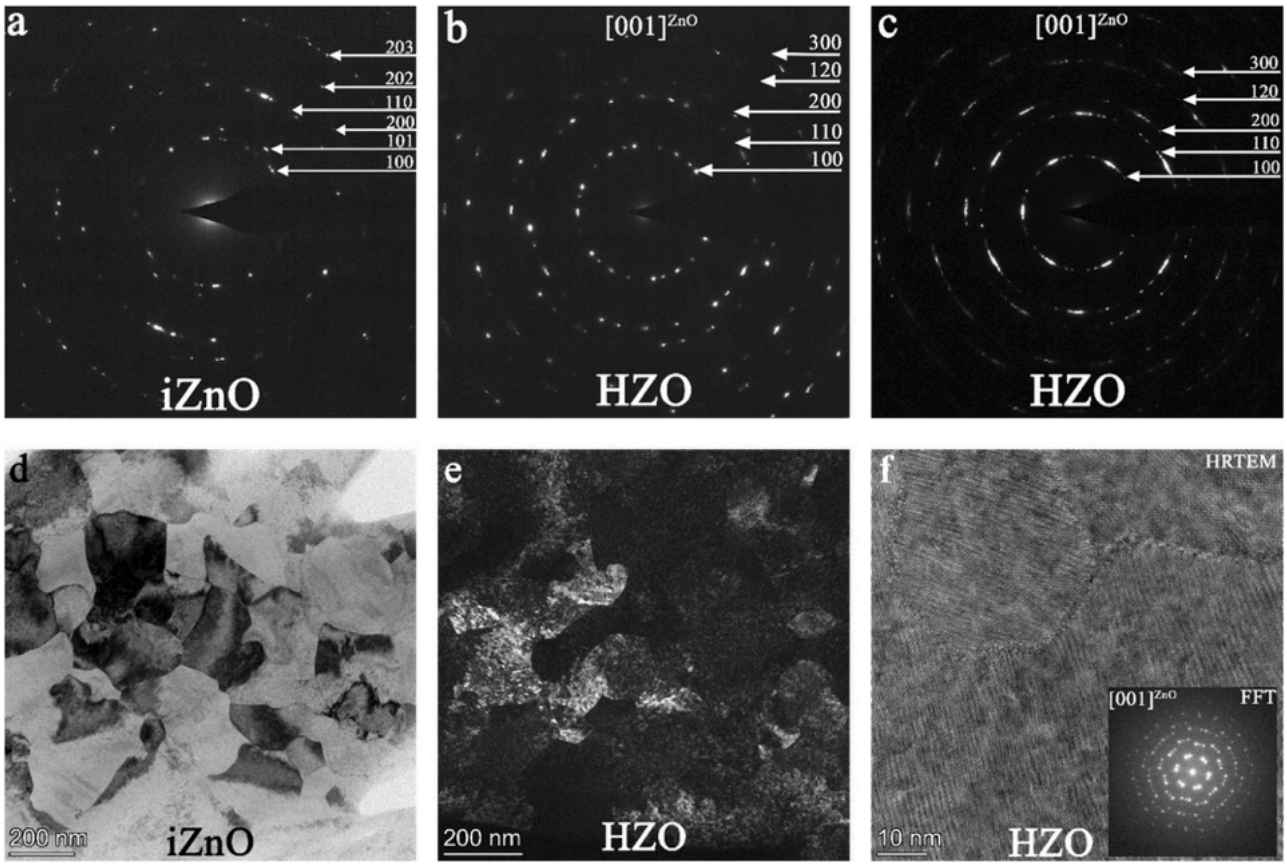


Fig. 7. a) Indexed SAED pattern from plan view sample of i-ZnO. Next to the typical reflections of the [001] zone, other reflections also appear, like 101, 202, 203, showing that the layer is less textured than the portion closer to the interface. b-c) Indexed SAED pattern from HZO acquired with the smallest selected area aperture and (b) with larger aperture (c) indicating a strongly textured layer, all the grains are in [001] projection with a slight rotation of each crystal around its c-axis. d) Bright field image from plan view TEM sample of i-ZnO showing the typical size and diameter of the ZnO columns in cross section. e) Dark field image from plan view TEM sample of HZO showing the typical size and diameter of the ZnO columns in cross sectional and the slight misorientation between the adjacent grains. f) HRTEM image with the corresponding FFT from plan view TEM sample of HZO confirm the strong texture in [001] projection: 3 grains (cross section of columns) with equilibrial ~120° triple grain boundary and the ~8.3° and ~16.6° low angle boundaries between individual grains.

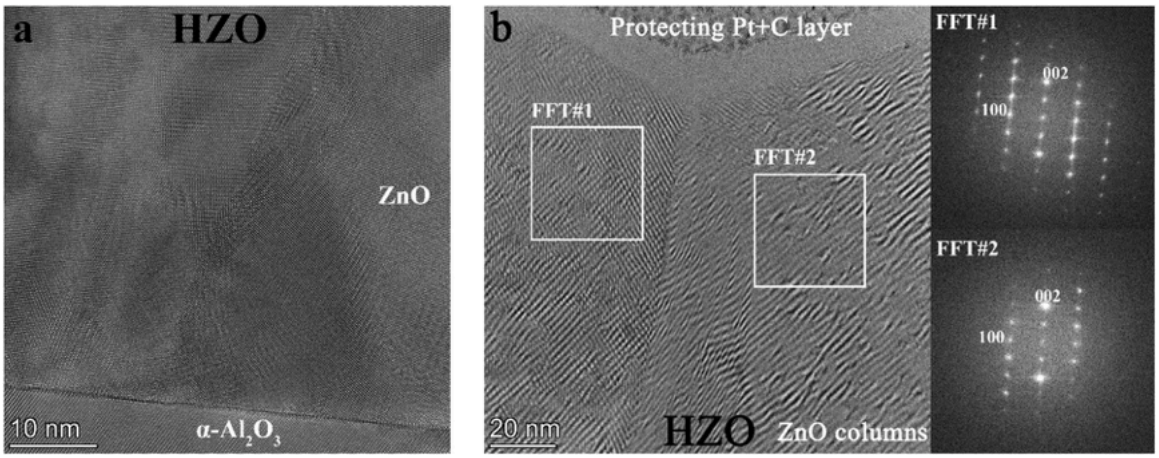


Fig. 8. HRTEM image from the interface region between the α-Al_2O_3 substrate and the HZO layer showing that most crystals are epitaxially grown on the substrate, and they overgrow the non-epitaxially grown crystals. b) HRTEM image highlighting the top region of two columnar HZO crystallites, showing that both of them are slightly rotated along their c directions.

well, and elemental mapping in STEM mode did not reveal chemically inhomogeneity like the presence of oxyhydroxide phases.

The comparison between i-ZnO and HZO focusses on an essential difference in crystallographic order, as clearly evidenced by the SAED experiments. This result unambiguously demonstrates that HZO possesses a significantly higher degree of crystalline order than i-ZnO. This structural condition strongly supports the interpretation that the B-M effect can be observed only in the HZO sample. Otherwise, the considerable lattice disorder in i-ZnO, localizes the impurity band, thus suppressing the manifestation of the B-M effect.

In summary, the structural and electrical properties of ZnO thin films were found to be strongly dependent on the reactive gas composition during sputtering process. In an Ar/O_2 atmosphere, the films exhibited high optical transparency, a smooth surface and poor crystallinity. Under these conditions, the carrier concentration was relatively high, but the low carrier mobility limited electrical transport. Scattering and disorder govern electron conduction (hopping), as reported for ZnO deposited under oxygen-rich condition [50,51].

An evident transition happened when a small partial pressure of water vapor was introduced into the sputtering chamber along with Ar and O_2.

Dissociation of H_2O under plasma conditions provides OH^- and H^+ radicals [52,53]. The -OH species can act as surfactants, enhancing adatom mobility at the growing surface and promoting preferential crystalline orientation. The effect is critically governed by the delicate balance of partial pressures between O_2 and H_2O. At the optimal condition, the oxygen partial pressure is enough to sustain stoichiometric ZnO growth, while the small addiction of water modifies the surface kinetics of the film during deposition without over-oxidizing the HZO.

3.2.4. DFT calculations

To investigate the energetics, surface structural morphology, and defect types that influence the HZO and i-ZnO layers, we performed spin-polarized DFT+U calculations using the Quantum Espresso suite of codes [54]. A plane-wave kinetic energy cutoff of 50 Ry and the standard solid-state pseudopotential (SSSP) library set optimized for the efficiency of the PBESol functional were used [55]. For the Hubbard-U correction [56], U values of 10 eV for Zn and 7.81 eV for O were adopted, ensuring consistency with the experimentally observed band gap of bulk ZnO. For HZO, the adsorption of water on the ZnO (0001) surface was modeled at various starting trial structures and monolayer (ML) coverages using a six-bilayer and a 3×3 surface cell slab model, separated by a vacuum spacing of at least 15 Å perpendicular to the surface, while a $2 \times 2 \times 1$ Monkhorst–Pack k-point mesh was used to sample the Brillouin zone. To account for the non-vanishing dipole density due to the surface asymmetry, dipole corrections were included in all surface calculations. For i-ZnO, neutral and charged defects, including oxygen vacancies (V_O), substitutional hydrogen at V_O (H_O), and Zn antisites (ZnO), were modeled in a $3 \times 3 \times 3$ supercell with a $5 \times 5 \times 3$ Monkhorst–Pack k-point mesh. All structural optimizations were performed until total energy and forces were converged to 1×10^{-4} and 1×10^{-3} a.u., respectively.

The model-predicted (and experimentally inferred) optimal coverage window discussed in paragraph 2.1 is supported by our DFT calculations. We find that at full coverage (1 ML), water is energetically more favorable in the molecular form when adsorbed on the Zn (0001) surface, with an adsorption energy of −0.034 eV/H_2O. The structure of the adsorbed water molecule at full coverage (not shown) consists of a bond distance of 2.27 Å between Zn (substrate) and O (H_2O), an intramolecular H–O bond distance of 0.96 Å, a Zn–O(H_2O)–Zn angle of 52.5°, and an H–O–H intramolecular angle of 112.8°. Instead, dissociative adsorption leading to the formation of an −OH hydroxyl group and H is energetically stabilized at lower coverages below ~0.3 ML, in agreement with earlier discussions of water adsorption on the ZnO surface [57,58]. This occurs because the dissociated species neutralize more of the unsaturated surface bonds, despite the additional energy required to break the water bond. The structure of the adsorption of OH and H species is shown in Fig. 1a for 0.11 ML coverage. The hydroxyl group bonds to a surface of Zn atoms with a Zn–O bond distance of 1.9 Å, while the H species bonds to a neighboring Zn atom at a distance of 2.6 Å. The covalent bond formation and charge transfer between the substrate and adsorbed species strongly influence the surface electronic band structure, inducing metallic conductivity (see Fig. 9a), with O and Zn states occupying the bandgap. This enhances the density of mobile carriers. Furthermore, our experimental data indicate that water adsorption (used to assist ZnO surface growth in the chamber) is dissociative, leaving hydroxyl groups on the surface. We also investigated using DFT the structural morphology and effects of the less energetically favorable hydroxyl adsorption at higher coverages of 0.5 and 1.0 ML. For the 0.5 ML coverage (Fig. 9b), the OH species is adsorbed at the surface Zn sites, while the H atom binds to the under-coordinated oxygen atoms at the edges, forming additional OH groups. In contrast, for the 1 ML

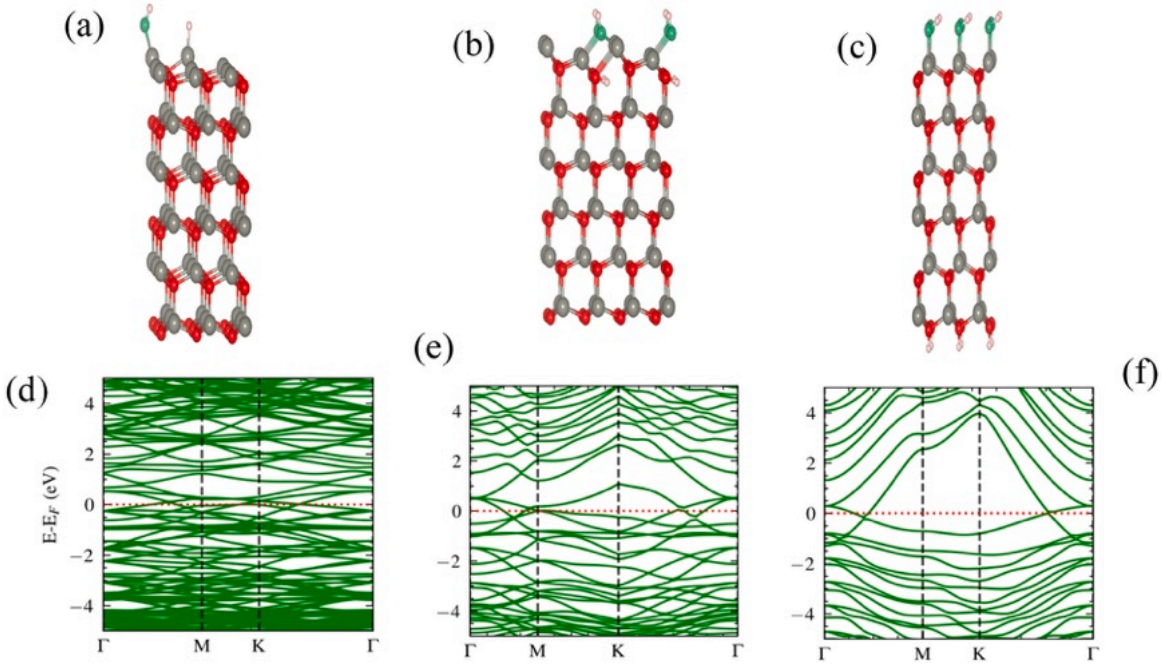


Fig. 9. Side view of DFT relaxed adsorption of the OH and H species on the Zn (0001), and the corresponding surface band structure for each surface for; (a) 0.11 ML coverage (calculations were performed in a 3 ×3 supercell), (b) 0.5 ML coverage (calculations were performed in a 2 ×1 supercell) and (c) full coverage (calculations were performed in a 1 ×1 cell), and the H specie were absorbed on the oxygen terminated $(000\bar{1})$surface. Grey, red, green and pink spheres represent, Zn, O, adsorbed O (of OH) and hydrogen respectively. Red dashed lines in the band structure plot indicates the Fermi energy shifted to zero.

coverage (Fig. 9c), the H atom bonds to the dangling oxygen at the oxygen-terminated$(000\bar{1})$surface, assuming that both Zn and O terminated surfaces are exposed in the chamber during growth. Both adsorption configurations have been reported to contribute to the stabilization of the polar Zn (0001) surface [59–61]. The surface band structures corresponding to these configurations further reveal the metallic conductivity of the Zn (0001) surface induced by OH and H adsorption. This finding is consistent with our experimental measurements of the HZO layer, where enhanced conductivity has been observed. In polycrystalline TCOs, carrier mobility is often limited by grain-boundary scattering and barrier formation rather than by intrinsic band dispersion alone. The DFT-calculated density of states (DOS Fig. 9) provides a microscopic picture consistent with the high carrier mobility measured in our HZO film. When the -OH coverage increases to 0.50 ML, we observe (i) a shift of the Fermi level toward/into the conduction band and (ii) an effective passivation of surface dangling bonds as also reflected by the relaxed surface geometries in Fig. 9. This chemical passivation reduces the density of surface states that can act as charged scattering centers and potential barriers, at the grain boundaries. Together with the micrometer-sized, c-axis-oriented grains observed in the TEM cross-sections, this decrease in grain-boundary barrier scattering supports the experimentally obtained mobility values (> 30 cm^2/Vs).

Furthermore, our experimental data indicate that water adsorption (used to assist ZnO surface growth in the chamber) is dissociative, leaving hydroxyl groups on the surface. We also investigated using DFT the structural morphology and effects of the less energetically favorable hydroxyl adsorption at higher coverages of 0.5 and 1.0 ML. For the 0.5 ML coverage (Fig. 9b), the OH species is adsorbed at the surface Zn sites, while the H atom binds to the under-coordinated oxygen atoms at the edges, forming additional OH groups. In contrast, for the 1 ML coverage (Fig. 9c), the H atom bonds to the dangling oxygen at the oxygen-terminated$(000\bar{1})$surface, assuming that both Zn and O terminated surfaces are exposed in the chamber during growth. Both adsorption configurations have been reported to contribute to the stabilization of the polar Zn (0001) surface [59–61]. The surface band structures corresponding to these configurations further reveal the metallic conductivity of the Zn (0001) surface induced by OH and H adsorption. This finding is consistent with our experimental measurements of the HZO layer, where enhanced conductivity has been observed.

In n-type ZnO, oxygen vacancies (V_O) are low-energy defects and would likely form in large concentrations. Our DFT results show that V_O thermally transits from the 2 + charge state to the neutral state, with a deep ε(2 +/0) level located 1.15 eV below the conduction band (see Fig. 10a), in agreement with the majority of earlier theoretical studies [62–65], but contrary to the shallow-donor behavior measured for i-ZnO. Thus, V_O is likely not the dominant source of carrier electrons, suggesting the presence of other defect types. This is a widely discussed problem in literature, and consequently, other shallow donor defects have been theoretically proposed as the origin of n-type conductivity in ZnO, including a metastable shallow donor state of V_O [66], Zn interstitials, Zn antisites, and substitutional hydrogen at the O vacancy site [63,64,67,68]. However, during the growth and annealing process, the i-ZnO layer is well protected and hydrogen is not present, thus leaving O vacancies and likely Zn defects as the possible donor candidates. Therefore, we have considered a defect complex consisting of a Zn antisite, where the Zn ion occupies the oxygen vacancy site. Even though this defect complex has a higher formation energy of −1.75 eV, compared to −2.50 eV for oxygen vacancies, it is expected to be stabilized by the presence of a very high concentration of oxygen vacancies [67] and by the thermal non-equilibrium conditions of the experiment. As shown in Fig. 10b, the Zn antisite behaves as a shallow donor, as the thermodynamic transition levels between the 2 +, 1 +, and neutral charge states occur beyond the conduction band minimum. This is due to the strong hybridization between the Zn antisite and the O vacancy, which modifies the electronic structure, lowers the formation energy, and leads to the formation of the shallow-donor state [67]. This is

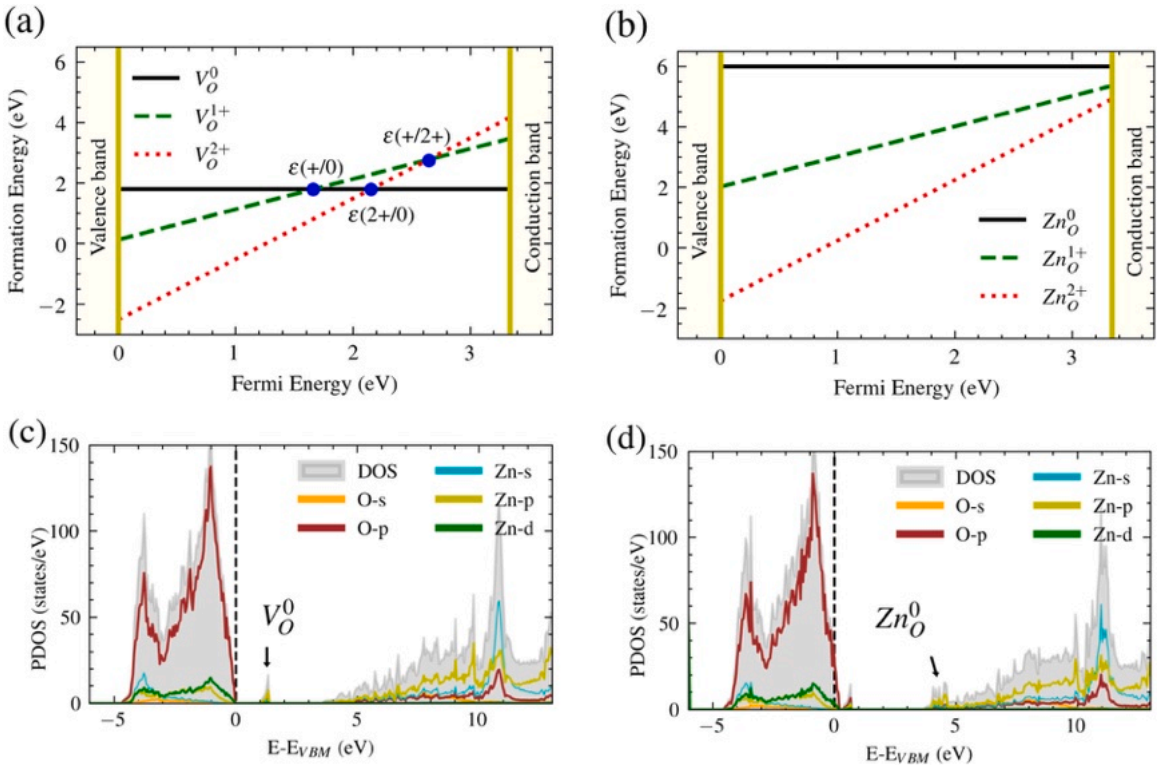


Fig. 10. Formation energy (in the Zinc-rich limit) vs Fermi level for neutral (0), 1 + and 2 + charged states for (a) oxygen vacancies (V_O), (b) zinc antisite (Zn_O) in ZnO. The projected density of states of the neutral charged states for (c) V_O^0 and (d) Zn_O^0.

consistent with the distribution of the density of states shown in Figs. 10c and 10d, where the O vacancy defect level lies deep in the band gap, far from the conduction-band minimum, whereas for the Zn antisite the defect level is located closer to the conduction-band minimum, accounting for the increased computed carrier concentration of ~10^{19} e/cm^3 and the improved conductivity measured experimentally. The existence of both deep and shallow donors in ZnO has been earlier reported and was utilized to explain the double thermal activation

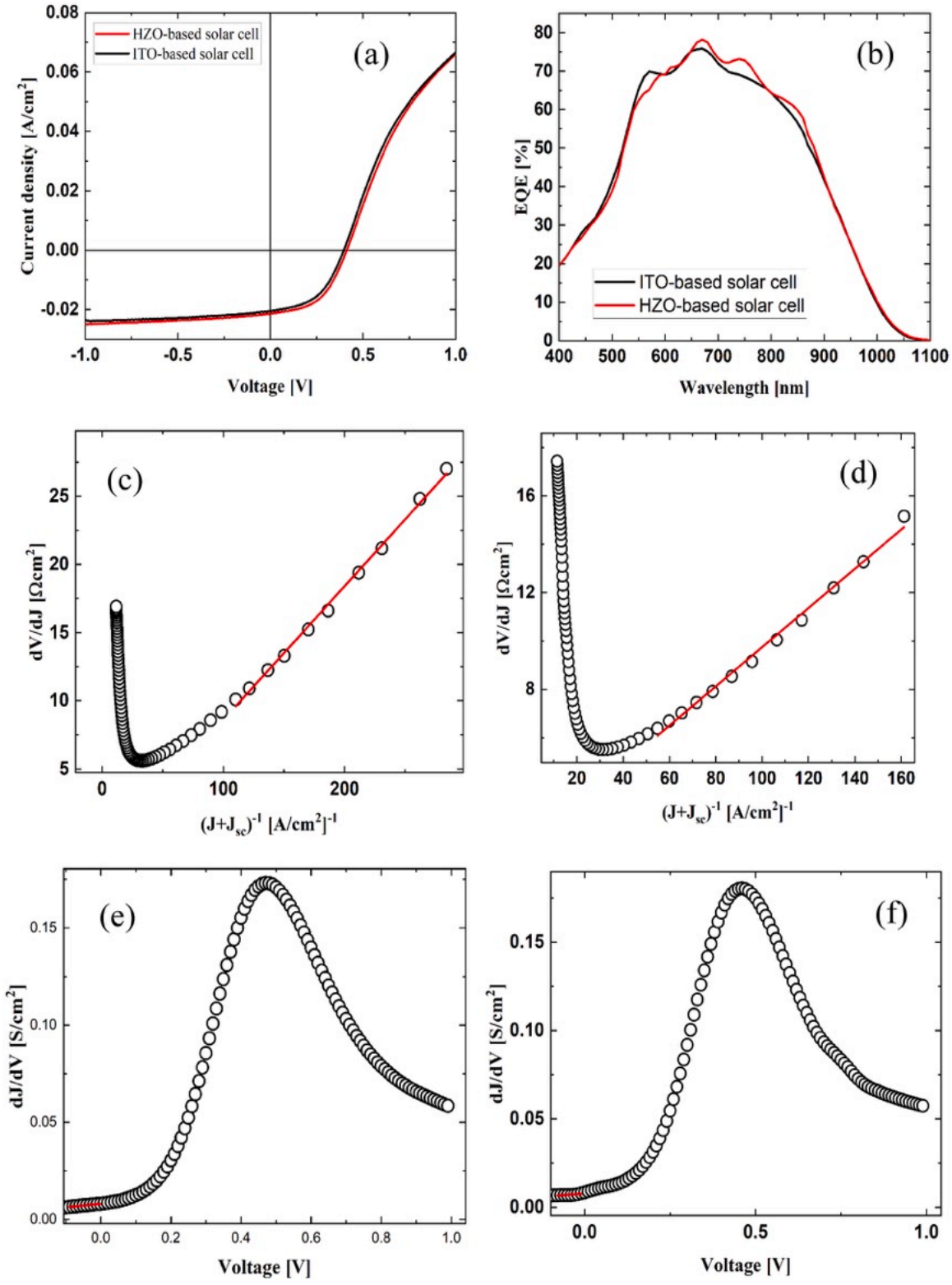


Fig. 11. (a) Current density–voltage (J–V) characteristics and (b) external quantum efficiency (EQE) spectra of the ITO-based and HZO-based solar cells. The J–V curves are measured under illumination (1KW/m^2, AM=1.5 G, T = 25°C), and the EQE spectra show the spectral response in the 400–1100 nm range. The oscillations arise from interference fringes within the TCO layers. The figures (c) and (d) represents the extrapolation of series resistance for HZO-based and ITO-based respectively. The figures (e) and (f) is possible to extract the shunt resistance.

conduction processes observed in ZnO [33]. This continues to show the indispensable role that oxygen vacancies play in the n-type conductivity of ZnO. Further, the Zn antisite relaxes into a reduced-symmetry configuration displaced by 0.51–0.63 Å from the ideal O vacancy site for the neutral to 2 + charge states, with the nearest-neighbor ZnO–Zn distance being ~2.4 Å, compared with the pristine O–Zn distance of 1.95 Å. Furthermore, this defect complex induces additional atomic displacements, likely producing substantial lattice relaxation, consistent with the large lattice disorder measured for i-ZnO.

Sb_2Se_3-based solar cell

Fig. 11 (a) illustrates a comparative analysis of Sb_2Se_3-based solar cells employing either the conventional TCO structure (900 nm ITO + 120 nm i-ZnO) or the novel HZO-based TCO as the front contact. The current–voltage (J-V) curves and the corresponding photovoltaic parameters, summarized in Table 2, exhibit comparable performance in both configurations. Batch statistics (N, mean ± SD) and the extracted R_s, R_{sh}(and R_s/R_{sh}) are summarized in Table 2. This outcome validates the potential of HZO as a viable alternative to conventional TCO layers.

To further investigate the impact of the HZO front contact on device performance, the series resistances were extracted from the J-V characteristics. As summarized in Table 2, the HZO-based cells exhibit a significant reduction in series resistance (R_s) from 1.66 ± 0.03 Ωcm^2 for the ITO reference to 1.21 ± 0.03 Ωcm^2. This decrease in R_s, coupled with a well-maintained shunt resistance (R_{sh}), accounts for the improvement in Fill Factor and suggests a more efficient charge carrier extraction at the TCO/buffer interface, likely due to a more favorable band alignment and reduced contact resistance compared to the standard ITO/i-ZnO bilayer.

The presence of a kink at high voltage in the first quadrant is attributed to an unfavorable band alignment between the window layer (CdS+ZnCdS) and the absorber (Sb_2Se_3), as previously reported in [69]. Additional confirmation is provided by the external quantum efficiency (EQE) spectra shown in Fig. 11(b), which are nearly identical for both devices, with a small but significant enhancement in the absorption observed when HZO is employed as the TCO, demonstrating good replaceability of the ITO layer with HZO. Notably, the EQE enhancement is mainly observed across the plateau region, while the short-wavelength response and the long-wavelength cut-off remain essentially unchanged. This wavelength-dependent signature is consistent with a light-management contribution (e.g., forward scattering and/or reduced parasitic optical losses) rather than a change in absorber band edge or junction collection physics. The J_{sc}values obtained by AM1.5 G integration of EQE agree with J–V within 0.2 %.

This result is confirmed from a TCO's figure of merit used for PV applications, expressed as [70]:

$$FoM = \frac{T^{10}}{R_s} \tag{26}$$

Where: T is the transmittance at 550 nm [0,1] and R_s is the sheet resistance [Ω/□]. The obtained values are FoM(ITO) = 0.025 and FoM (HZO) = 0.022. This result strongly suggests a good substitution between ITO and HZO.

These experimental observations have insightful significance: HZO as TCO can be used in the production of solar cells, avoiding the use of ITO, which can lead to free carrier absorption, resulting in absorption in the visible part of the near-infrared spectrum, or the use of ZnO heavily doped with Al, or B, with the consequent possibility of diffusion of dopant species when heated to high temperatures. By using HZO, experimentation has also highlighted that the use of a high-resistivity layer (HRL) is unnecessary, as it eliminates the need to shield the diffusion of dopant species (In and Sn from ITO and Al, B from AZO; BZO).

Table 2
PV parameters of solar cells based on ITO+iZnO and HZO TCOs. Ten cells were tested for each batch (HZO-based and ITO-based). The reported values are the mean and standard deviation.

	ITO-based	HZO-based
J_{sc} [mA/cm^2]	20.47 ± 0.02	21.25 ± 0.03
V_{oc} [mV]	395.9 ± 1.1	413.1 ± 1.4
FF	0.48 ± 0.01	0.49 ± 0.01
PCE [%]	3.89 ± 0.04	4.31 ± 0.04
R_s [Ωcm^2]	1.66 ± 0.03	1.21 ± 0.03
R_{sh} [Ωcm^2]	126.8 ± 0.6	124.1 ± 1.3
R_s/R_{sh}	(13.1 ± 0.3) * 10^{-3}	(9.8 ± 0.3) * 10^{-3}

4. Conclusion

We introduce a H_2O-assisted ZnO (HZO)-based TCO grown by reactive d.c. magnetron sputtering in an Ar/O_2/H_2O atmosphere and explain its growth-property link with a coupled discharge and surface kinetics model. A controlled H_2O dosage establishes a chemisorbed –OH coverage, on the substrate surface, that acts as a surfactant The pulsed d.c. mode stabilizes the discharge and decouples the growth rate control from that of the microstructure. The model links power density, H_2O fraction, and temperature to the metallicity index and steady-state –OH coverage, identifying an operating window and promotes c-oriented columnar grains at the micrometer scale. These results are in full agreement with the DFT calculation. Furthermore, the DFT predictions for the defects responsible for conductivity in HZO and i-ZnO are consistent with the literature. Optically, HZO exhibits high transparency in the visible range of the solar spectrum with $E_g \approx 3.28$ eV and a ≈ 10 % increase in the surface diffuse-fraction proxy compared to i-ZnO, useful for light management in superstrate solar cells. Electrically, HZO is in the degenerate regime with $\mu_e > 30$ cm^2 V^{-1} s^{-1} , n ≈ 10^{19} cm^{-3} ; a slight optical blue-shift is consistent with a Burstein–Moss effect partially compensated by band-gap renormalization. At device level, used as a front contact in Sb_2Se_3 cells, HZO matches or surpasses the conventional ITO+i-ZnO stack, consistent with the TCO figure of merit and the slight EQE gain. This result is particularly significant as it demonstrates that high-performance photovoltaics can be achieved by replacing rare and expensive Indium-based compounds with a single-layer, earth-abundant oxide without compromising carrier collection efficiency. In addition to performance parity, HZO avoids the known ITO/AZO criticalities (free carrier absorption, In/Al diffusion), allowing for stack simplification without dedicated HRL layers.

Compared to recent literature on multi-element co-doping (e.g., Al-B or Al-Ga co-doped ZnO), which often requires complex targets, our HZO approach achieves competitive mobility (> 30 cm^{2}V^{-1}s^{-1}) through a simpler single-target sputtering process. When integrated into Sb_2Se_3 solar cells, HZO acts as an effective window and yields a slight EQE gain consistent with enhanced light scattering, which is particularly beneficial for the Sb_2Se_3 absorber near its band edge.

Combining low-cost scalability (stable process window), non-critical elements and premium optoelectronic properties, HZO promises to be a next-generation TCO for thin-film photovoltaics, with expected benefits in terms of reliability, sustainability and industrial integration.

CRediT authorship contribution statement

Ildikò Cora: Writing – review & editing, Visualization, Validation, Investigation, Formal analysis, Data curation. **Gianluca Foti:** Writing – review & editing, Writing – original draft, Visualization, Data curation. **Donato Spoltore:** Writing – review & editing, Validation. **Stefano Pasini:** Writing – review & editing, Writing – original draft, Visualization, Investigation, Formal analysis, Data curation. **Alessio Bosio:** Writing – review & editing, Writing – original draft, Validation, Supervision, Methodology, Funding acquisition, Conceptualization. **Andrea Baraldi:** Writing – review & editing, Validation, Investigation, Data

curation. **Francesco Mezzadri:** Writing – review & editing, Validation, Methodology, Formal analysis. **Ifeanyi John Onuorah:** Writing – original draft, Visualization, Software, Investigation, Data curation. **Muhammad Kashif:** Writing – review & editing, Visualization. **Samaneh Shapouri:** Writing – review & editing, Visualization. **Giovanna Sozzi:** Writing – review & editing, Validation, Conceptualization. **Antonella Parisini:** Writing – review & editing, Validation, Supervision, Methodology, Formal analysis, Conceptualization. **Béla Pécz:** Writing – review & editing, Validation, Supervision, Funding acquisition, Conceptualization.

Declaration of Competing Interest

The authors declare that they have no known competing financial interests or personal relationships that could have appeared to influence the work reported in this paper.

Acknowledgment

This research was funded by the National Recovery and Resilience Plan (NRRP), Mission 4 Component 2 Investment 1.5—Call for tender No. 3277 of 30/12/2021 of the Italian Ministry of University and Research funded by the European Union—NextGenerationEU. Award Number: Project code ECS00000033, Concession Decree No. 1052 of 23/06/2022 adopted by the Italian Ministry of University and Research, CUP D93C22000460001, "Ecosystem for Sustainable Transition in Emilia-Romagna" (Ecosister). This research was supported by CET-Partnership, the Clean Energy Transition Partnership under the 20XX joint call for research proposals, and by the European Commission (GA N°101069750) and with the organizations detailed on https://cetpartnership.eu/funding- agencies-and-call-mod-ules.

Authors are grateful for VEKOP-2.3.3–15–2016–00002 of the European Structural and Investment Funds for their support and also thank the Ministry of Innovation and Technology of Hungary from the National Research, Development and Innovation Fund, financed under the TKP2021 funding scheme (Grants TKP2021-NVA-03 and TKPS2021-NKTA-05). I.Cora is grateful for the János Bolyai Research Scholarship of the Hungarian Academy of Sciences for their support. Authors gratefully thank Noémi Szász for the TEM sample preparations and Salvatore Vantaggio for the electrical measurements related to the Hall effect.

References

[1] E. Chan, Y. Díaz, J.M. Camacho, A. Duarte-Moller, R. Castro-Rodríguez, P. Bartolo-Pérez, Influence of the oxygen pressure on the physical properties of the pulsed-laser deposited Te doped SnO2 thin films, J. Alloy. Compd. 508 (2010) 342–347, https://doi.org/10.1016/j.jallcom.2010.08.076.

[2] A.N. Banerjee, K.K. Chattopadhyay, Recent developments in the emerging field of crystalline p-type transparent conducting oxide thin films, Prog. Cryst. Growth Charact. Mater. 50 (2005) 52–105, https://doi.org/10.1016/j.pcrysgrow.2005.10.001.

[3] S.J. Ikhmayies, Transparent conducting oxides for solar cell applications, in: Mediterranean Green Buildings and Renewable Energy: Selected Papers from the World Renewable Energy Network's Med Green Forum, Springer International Publishing, 2017, pp. 899–907, https://doi.org/10.1007/978-3-319-30746-6_70.

[4] A. Bosio, S. Pasini, N. Romeo, The history of photovoltaics with emphasis on CdTe solar cells and modules, Coatings 10 (2020), https://doi.org/10.3390/coatings10040344.

[5] T.S. Moss, The Interpretation of the Properties of Indium Antimonide, n.d.

[6] D. Ginley, D. Paine, Handbook of Transparent Conductors, Springer, US, 2011, https://doi.org/10.1007/978-1-4419-1638-9.

[7] M. Frenzel, C. Mikolajczak, M.A. Reuter, J. Gutzmer, Quantifying the relative availability of high-tech by-product metals – The cases of gallium, germanium and indium, Resour. Policy 52 (2017) 327–335, https://doi.org/10.1016/j.resourpol.2017.04.008.

[8] D.H. Zhang, H.L. Ma, Scattering mechanisms of charge carriers in transparent conducting oxide films, Appl. Phys. A Mater. Sci. Process 62 (1996) 487–492, https://doi.org/10.1007/BF01567122.

[9] T. Minami, Substitution of transparent conducting oxide thin films for indium tin oxide transparent electrode applications, Thin Solid Films 516 (2008) 1314–1321, https://doi.org/10.1016/j.tsf.2007.03.082.

[10] S. Pasini, D. Spoltore, A. Parisini, S. Marchionna, L. Fornasini, D. Bersani, R. Fornari, A. Bosio, Innovative back-contact for Sb2Se3 -based thin film solar cells, Sol. Energy 249 (2023) 414–423, https://doi.org/10.1016/j.solener.2022.11.049.

[11] L. Znaidi, Sol–gel-deposited ZnO thin films: A review, Materials Science Engineering B 174 (2010) 18–30, https://doi.org/10.1016/j.mseb.2010.07.001.

[12] E. Guziewicz, M. Godlewski, L. Wachnicki, T.A. Krajewski, G. Luka, S. Gieraltowska, R. Jakiela, A. Stonert, W. Lisowski, M. Krawczyk, J.W. Sobczak, A. Jablonski, ALD grown zinc oxide with controllable electrical properties, Semicond. Sci. Technol. 27 (2012) 074011, https://doi.org/10.1088/0268-1242/27/7/074011.

[13] P.J. Kelly, R.D. Arnell, Magnetron sputtering: a review of recent developments and applications, Vacuum 56 (2000) 159–172, https://doi.org/10.1016/S0042-207X(99)00189-X.

[14] S. Pasini, D. Spoltore, A. Parisini, G. Foti, S. Marchionna, S. Vantaggio, R. Fornari, A. Bosio, Sb2Se3 Polycrystalline Thin Films Grown on Different Window Layers, Coatings 13 (2023), https://doi.org/10.3390/coatings13020338.

[15] V.I. Shapovalov, Modeling of Reactive Sputtering—History and Development, Materials 16 (2023) 3258, https://doi.org/10.3390/ma16083258.

[16] S. Berg, T. Nyberg, Fundamental understanding and modeling of reactive sputtering processes, Thin Solid Films 476 (2005) 215–230, https://doi.org/10.1016/j.tsf.2004.10.051.

[17] I. Langmuir, The Adsorption Of Gases On Plane Surfaces Of Glass, Mica And Platinum, J. Am. Chem. Soc. 40 (1918) 1361–1403, https://doi.org/10.1021/ja02242a004.

[18] R. Gomer, Diffusion of adsorbates on metal surfaces, Rep. Prog. Phys. 53 (1990) 917–1002, https://doi.org/10.1088/0034-4885/53/7/002.

[19] M.B. Hugenschmidt, L. Gamble, C.T. Campbell, The interaction of H2O with a TiO2 (110) surface, Surf. Sci. 302 (1994) 329–340, https://doi.org/10.1016/0039-6028(94)90837-0.

[20] Y. Zhang, H. Wang, L. Huang, J. Chen, C. Wu, K. Nie, Y. Liang, Z. Wang, Q. Zhang, Orbital hybridization-guided BiOX (X = F, Cl, Br, I) photocatalysts: halogen-induced bandgap engineering and performance optimization, Mater. Lett. 405 (2026), https://doi.org/10.1016/j.matlet.2025.139824.

[21] W. Chen, Y. Liang, Z. Chen, Y. Zhang, J. Wang, X. Chen, C. Zhou, K. Nie, Z. Wang, Q. Zhang, Dual NPN Bi2O3/BiOCl/Bi24O31Cl10 ternary heterojunction for the enhanced photocatalytic activities, J. Alloy. Compd. 1027 (2025), https://doi.org/10.1016/j.jallcom.2025.180561.

[22] H. Fujiwara, Spectroscopic Ellipsometry, Wiley, 2007, https://doi.org/10.1002/9780470060193.

[23] H.A. Macleod, Thin-film optical filters, CRC Press, Taylor & Francis, 2010.

[24] A. Yang, X. Bao, S. Li, R. Yang, T. Wang, Y. Wang, L. Sun, Nano-ZnO film preparation at low temperature and the optical indices calculation, Optoelectron. Lett. 10 (2014) 216–220, https://doi.org/10.1007/s11801-014-4034-6.

[25] A.B. Djurišić, E.H. Li, Modeling the optical properties of sapphire (α-Al2O3 (https://doi.org/), Opt. Commun. 157 (1998) 72–76, https://doi.org/10.1016/S0030-4018(98)00503-3.

[26] R.F. Pierret, Advanced Semiconductor Fundamentals, Second, Prentice Hall, 2003. ⟨https://books.google.it/books?id=d2hrQgAACAAJ⟩ (accessed May 6, 2025).

[27] M. Oshikiri, Y. Imanaka, F. Aryasetiawan, G. Kido, Comparison of the electron effective mass of the n-type ZnO in the wurtzite structure measured by cyclotron resonance and calculated from first principle theory, Phys. B Condens. Matter 298 (2001) 472–476, https://doi.org/10.1016/S0921-4526(01)00365-9.

[28] S.V. Vegesna, V.J. Bhat, D. Bürger, J. Dellith, I. Skorupa, O.G. Schmidt, H. Schmidt, Increased static dielectric constant in ZnMnO and ZnCoO thin films with bound magnetic polarons, Sci. Rep. 10 (2020) 6698, https://doi.org/10.1038/s41598-020-63195-1.

[29] A. Bosio, A. Parisini, A. Lamperti, C. Borelli, L. Fornasini, M. Bosi, I. Cora, Z. Fogarassy, B. Pécz, Z. Zolnai, A. Németh, S. Vantaggio, R. Fornari, n-Type doping of ε-Ga_2O_3 epilayers by high-temperature tin diffusion, Acta Mater. 210 (2021) 116848, https://doi.org/10.1016/j.actamat.2021.116848.

[30] A. Parisini, A. Parisini, R. Nipoti, Size effect on high temperature variable range hopping in Al+ implanted 4H-SiC, J. Phys. Condens. Matter 29 (2017), https://doi.org/10.1088/1361-648X/29/3/035703.

[31] A. Parisini, M. Gorni, A. Nath, L. Belsito, M.V. Rao, R. Nipoti, Remarks on the room temperature impurity band conduction in heavily Al+ implanted 4H-SiC, J. Appl. Phys. 118 (2015), https://doi.org/10.1063/1.4926751.

[32] N.F. Mott, Conduction in non-crystalline systems, Philos. Mag. 17 (1968) 1259–1268, https://doi.org/10.1080/14786436808223200.

[33] C.C. Lien, C.Y. Wu, Z.Q. Li, J.J. Lin, Electrical conduction processes in ZnO in a wide temperature range 20–500 K, J. Appl. Phys. 110 (2011), https://doi.org/10.1063/1.3638120.

[34] Y.-L. Huang, S.-P. Chiu, Z.-X. Zhu, Z.-Q. Li, J.-J. Lin, Variable-range-hopping conduction processes in oxygen deficient polycrystalline ZnO films, J. Appl. Phys. 107 (2010), https://doi.org/10.1063/1.3357376.

[35] A. Di Trolio, A.M. Testa, A. Amore Bonapasta, Role of the carrier density in the transport mechanisms of polycrystalline ZnO films, Phys. Chem. Chem. Phys. 23 (2021) 13918–13925, https://doi.org/10.1039/D1CP01612A.

[36] B.T. Benton, B.L. Greenberg, E. Aydil, U.R. Kortshagen, S.A. Campbell, Variable range hopping conduction in ZnO nanocrystal thin films, Nanotechnology 29 (2018) 415202, https://doi.org/10.1088/1361-6528/aad6ce.

[37] T.T. Lin, S.L. Young, C.Y. Kung, H.Z. Chen, M.C. Kao, M.C. Chang, C.R. Ou, Variable-Range Hopping and Thermal Activation Conduction of Y-Doped ZnO Nanocrystalline Films, IEEE Trans. Nanotechnol. 13 (2014) 425–430, https://doi.org/10.1109/TNANO.2013.2280648.

[38] M. Feneberg, S. Osterburg, K. Lange, C. Lidig, B. Garke, R. Goldhahn, E. Richter, C. Netzel, M.D. Neumann, N. Esser, S. Fritze, H. Witte, J. Bläsing, A. Dadgar,

A. Krost, Band gap renormalization and Burstein-Moss effect in silicon- and germanium-doped wurtzite GaN up to 10^20cm^-3, Phys. Rev. B 90 (2014) 075203, https://doi.org/10.1103/PhysRevB.90.075203.
[39] A. Walsh, J.L.F. Da Silva, S.H. Wei, Origins of band-gap renormalization in degenerately doped semiconductors, Phys. Rev. B Condens. Matter Mater. Phys. 78 (2008), https://doi.org/10.1103/PhysRevB.78.075211.
[40] J.A. Reyes, M. del Castillo-Mussot, Wannier-Mott exciton formed by electron and hole separated in parallel quantum wires, Phys. Rev. B 57 (1998) 1690–1697, https://doi.org/10.1103/PhysRevB.57.1690.
[41] M. Grunert, M. Großmann, E. Runge, Predicting exciton binding energies from ground-state properties, Phys. Rev. B 110 (2024), https://doi.org/10.1103/PhysRevB.110.075204.
[42] X. Zhang, X. Qian, J. Tang, N. Zhu, Z. Li, J. Fu, L. Li, Y. Wang, Effect of polar/non-polar facets on the transformation of nanoscale ZnO in simulated sweat and potential impacts on the antibacterial activity, Ecotoxicol. Environ. Saf. 246 (2022), https://doi.org/10.1016/j.ecoenv.2022.114187.
[43] D.P. Norton, Y.W. Heo, M.P. Ivill, K. Ip, S.J. Pearton, M.F. Chisholm, T. Steiner, ZnO: growth, doping & processing, Mater. Today 7 (2004) 34–40, https://doi.org/10.1016/S1369-7021(04)00287-1.
[44] Ü. Özgür, Ya.I. Alivov, C. Liu, A. Teke, M.A. Reshchikov, S. Doğan, V. Avrutin, S.-J. Cho, H. Morkoç, A comprehensive review of ZnO materials and devices, J. Appl. Phys. 98 (2005) 041301, https://doi.org/10.1063/1.1992666.
[45] H. Morkoç, Ü. Özgür, Optical Properties, in: Zinc Oxide, 2009: pp. 131–244. https://doi.org/⟨https://doi.org/10.1002/9783527623945.ch3⟩.
[46] T. Siegrist, P. Jost, H. Volker, M. Woda, P. Merkelbach, C. Schlockermann, M. Wuttig, Disorder-induced localization in crystalline phase-change materials, Nat. Mater. 10 (2011) 202–208, https://doi.org/10.1038/nmat2934.
[47] M. Gurvitch, Ioffe-Regel criterion and resistivity of metals, 1981. ⟨https://doi.org/10.1103/PhysRevB.24.7404⟩.
[48] S. Pasini, D. Spoltore, A. Parisini, G. Foti, S. Marchionna, S. Vantaggio, R. Fornari, A. Bosio, Sb_2Se_3 Polycrystalline Thin Films Grown on Different Window Layers, Coatings 13 (2023) 338, https://doi.org/10.3390/coatings13020338.
[49] G.B. Harris, X. Quantitative measurement of preferred orientation in rolled uranium bars, Lond. Edinb. Dublin Philos. Mag. J. Sci. 43 (1952) 113–123, https://doi.org/10.1080/14786440108520972.
[50] D.C. Look, Recent advances in ZnO materials and devices, Materials Science Engineering B 80 (2001) 383–387, https://doi.org/10.1016/S0921-5107(00)00604-8.
[51] T. Minami, Transparent conducting oxide semiconductors for transparent electrodes, Semicond. Sci. Technol. 20 (2005) S35, https://doi.org/10.1088/0268-1242/20/4/004.
[52] M.A. Lieberman, A.J. Lichtenberg, Principles of Plasma Discharges and Materials Processing, Wiley, 2005, https://doi.org/10.1002/0471724254.
[53] J. Hopwood, Review of inductively coupled plasmas for plasma processing, Plasma Sources Sci. Technol. 1 (1992) 109, https://doi.org/10.1088/0963-0252/1/2/006.
[54] P. Giannozzi, S. Baroni, N. Bonini, M. Calandra, R. Car, C. Cavazzoni, D. Ceresoli, G.L. Chiarotti, M. Cococcioni, I. Dabo, A. Dal Corso, S. de Gironcoli, S. Fabris, G. Fratesi, R. Gebauer, U. Gerstmann, C. Gougoussis, A. Kokalj, M. Lazzeri, L. Martin-Samos, N. Marzari, F. Mauri, R. Mazzarello, S. Paolini, A. Pasquarello, L. Paulatto, C. Sbraccia, S. Scandolo, G. Sclauzero, A.P. Seitsonen, A. Smogunov, P. Umari, R.M. Wentzcovitch, QUANTUM ESPRESSO: a modular and open-source software project for quantum simulations of materials, J. Phys. Condens. Matter 21 (2009) 395502, https://doi.org/10.1088/0953-8984/21/39/395502.
[55] G. Prandini, A. Marrazzo, I.E. Castelli, N. Mounet, N. Marzari, Precision and efficiency in solid-state pseudopotential calculations, NPJ Comput. Mater. 4 (2018) 72, https://doi.org/10.1038/s41524-018-0127-2.
[56] V.I. Anisimov, J. Zaanen, O.K. Andersen, Band theory and Mott insulators: Hubbard *U* instead of Stoner *I*, Phys. Rev. B 44 (1991) 943–954, https://doi.org/10.1103/PhysRevB.44.943.
[57] H. Ye, G. Chen, H. Niu, Y. Zhu, L. Shao, Z. Qiao, Structures and Mechanisms of Water Adsorption on ZnO(0001) and GaN(0001) Surface, J. Phys. Chem. C. 117 (2013) 15976–15983, https://doi.org/10.1021/jp312847r.
[58] Y. Liu, W. Xu, Y. Shan, H. Xu, High Reactivity of the ZnO(0001) Polar Surface: The Role of Oxygen Adatoms, J. Phys. Chem. C. 121 (2017) 15711–15718, https://doi.org/10.1021/acs.jpcc.7b03326.
[59] A. Önsten, D. Stoltz, P. Palmgren, S. Yu, M. Göthelid, U.O. Karlsson, Water Adsorption on ZnO(0001): Transition from Triangular Surface Structures to a Disordered Hydroxyl Terminated phase, J. Phys. Chem. C. 114 (2010) 11157–11161, https://doi.org/10.1021/jp1004677.
[60] A. Wander, N.M. Harrison, The stability of polar oxide surfaces: The interaction of H2O with ZnO(0001) and ZnO(000ª, J. Chem. Phys. 115 (2001) 2312–2316, https://doi.org/10.1063/1.1384030.
[61] G. Kresse, O. Dulub, U. Diebold, Competing stabilization mechanism for the polar ZnO(0001)-Zn surface, Phys. Rev. B 68 (2003) 245409, https://doi.org/10.1103/PhysRevB.68.245409.
[62] A. Janotti, C.G. Van de Walle, Oxygen vacancies in ZnO, Appl. Phys. Lett. 87 (2005) 122102, https://doi.org/10.1063/1.2053360.
[63] A. Janotti, C.G. Van de Walle, Native point defects in ZnO, Phys. Rev. B 76 (2007) 165202, https://doi.org/10.1103/PhysRevB.76.165202.
[64] C.G. Van de Walle, Hydrogen as a Cause of Doping in Zinc Oxide, Phys. Rev. Lett. 85 (2000) 1012–1015, https://doi.org/10.1103/PhysRevLett.85.1012.
[65] J. Buckeridge, C.R.A. Catlow, M.R. Farrow, A.J. Logsdail, D.O. Scanlon, T.W. Keal, P. Sherwood, S.M. Woodley, A.A. Sokol, A. Walsh, Deep vs shallow nature of oxygen vacancies and consequent <math> <mi>n</mi> </math> -type carrier concentrations in transparent conducting oxides, Phys. Rev. Mater. 2 (2018) 054604, https://doi.org/10.1103/PhysRevMaterials.2.054604.
[66] S. Lany, A. Zunger, Anion vacancies as a source of persistent photoconductivity in II-VI and chalcopyrite semiconductors, Phys. Rev. B 72 (2005) 035215, https://doi.org/10.1103/PhysRevB.72.035215.
[67] Y.-S. Kim, C.H. Park, Rich Variety of Defects in ZnO via an Attractive Interaction between O Vacancies and Zn Interstitials: Origin of <math display="inline"> <mi>n</mi> </math> -Type Doping, Phys. Rev. Lett. 102 (2009) 086403, https://doi.org/10.1103/PhysRevLett.102.086403.
[68] F. Oba, A. Togo, I. Tanaka, J. Paier, G. Kresse, Defect energetics in ZnO: A hybrid Hartree-Fock density functional study, Phys. Rev. B 77 (2008) 245202, https://doi.org/10.1103/PhysRevB.77.245202.
[69] A. Bosio, S. Pasini, D. Spoltore, G. Foti, A. Parisini, M. Pavesi, S. Shapouri, I. Cora, Z. Fogarassy, R. Fornari, Effect of Heterojunction Characteristics and Deep Electronic Levels on the Performance of (Cd,Zn)S/Sb2Se3 Solar Cells, Appl. Sci. 15 (2025) 2930, https://doi.org/10.3390/app15062930.
[70] G. Haacke, New figure of merit for transparent conductors, J. Appl. Phys. 47 (1976) 4086–4089, https://doi.org/10.1063/1.323240.